

# On the origin of gamma rays in *Fermi* blazars: beyond the broad line region.

L. Costamante<sup>1,2,3</sup> , S. Cutini<sup>4,5</sup>, G. Tosti<sup>3</sup>, E. Antolini<sup>3</sup>, A. Tramacere<sup>6</sup>

<sup>1</sup>ASI – Unità di Ricerca Scientifica, Via del Politecnico snc, I-00133, Roma, Italy

<sup>2</sup>INAF – Osservatorio Astronomico di Brera, via E. Bianchi 46, I-23807 Merate, Italy

<sup>3</sup>Dipartimento di Fisica e Geologia, Università degli Studi di Perugia, via Pascoli snc, I-06123 Perugia, Italy

<sup>4</sup>ASI – Science Data Center, Via del Politecnico snc, I-00133, Roma, Italy

<sup>5</sup>INFN – Sezione di Perugia, Via Pascoli snc, I-06123, Perugia, Italy

<sup>6</sup>ISDC – Department of Astronomy, University of Geneva, 16, 1290 Versoix, Switzerland

Accepted 2018 April 4. Received 2018 April 4; in original form 2017 December 7.

## ABSTRACT

The gamma-ray emission in broad-line blazars is generally explained as inverse Compton (IC) radiation of relativistic electrons in the jet scattering optical-UV photons from the Broad Line Region (BLR), the so-called BLR External Compton scenario. We test this scenario on the *Fermi* gamma-ray spectra of 106 broad-line blazars detected with the highest significance or largest BLR, by looking for cut-off signatures at high energies compatible with  $\gamma$ - $\gamma$  interactions with BLR photons. We do not find evidence for the expected BLR absorption. For 2/3 of the sources, we can exclude any significant absorption ( $\tau_{\max} < 1$ ), while for the remaining 1/3 the possible absorption is constrained to be 1.5–2 orders of magnitude lower than expected. This result holds also dividing the spectra in high and low-flux states, and for powerful blazars with large BLR. Only 1 object out of 10 seems compatible with substantial attenuation ( $\tau_{\max} > 5$ ). We conclude that for 9 out of 10 objects, the jet does not interact with BLR photons. Gamma-rays seem either produced outside the BLR most of the time, or the BLR is  $\sim 100\times$  larger than given by reverberation mapping. This means that i) External Compton on BLR photons is disfavoured as the main gamma-ray mechanism, vs IC on IR photons from the torus or synchrotron self-Compton; ii) the *Fermi* gamma-ray spectrum is mostly intrinsic, determined by the interaction of the particle distribution with the seed-photons spectrum; iii) without suppression by the BLR, broad-line blazars can become copious emitters above 100 GeV, as demonstrated by 3C 454.3. We expect the CTA sky to be much richer of broad-line blazars than previously thought.

**Key words:** Galaxies: active – quasars: general – galaxies: jets – gamma rays: general

## 1 INTRODUCTION

The location of the main gamma-ray emitting region in blazars – the so-called “blazar zone” – is still rather uncertain, even though the gamma-ray emission often dominates their entire spectral energy distribution (SED). Blazars are usually divided into flat spectrum radio quasars (FSRQ) and BL Lac objects, according to the presence or absence of strong broad emission lines in their UV-optical spectra (Urry & Padovani 1995). This often corresponds to a different regime of accretion, with most gamma-ray bright FSRQ having a luminous, radiatively efficient accretion disc (Ghisellini et al. 2011b; Sbarrato et al. 2012).

In FSRQ the jet is then expected to propagate through dense regions of radiation, produced by gas reprocessing the disc emis-

sion at different distances from the black hole (BH), like UV-optical emission lines and recombination continua from the broad line region (BLR, Peterson 2006) and thermal IR radiation from the inner parts of the AGN dusty torus. Reverberation mapping studies in both radio-quiet and radio-loud objects indicate that the size of the BLR and dusty torus scales with the disc luminosity  $L_d$  as  $R \propto L_d^{1/2}$ , namely as  $R_{\text{BLR}} \simeq 0.1 L_{d,46}^{1/2}$  pc (Bentz et al. 2006; Kaspi et al. 2007) and  $R_{\text{IR}} \simeq 2.5 L_{d,46}^{1/2}$  pc (Cleary et al. 2007; Nenkova et al. 2008), respectively (where we use the notation  $L_{d,x}$  for  $L_d$  in units of  $10^x$  erg s<sup>-1</sup>). The resulting energy density  $U_{\text{ext}} \propto L_d/R^2 c$  should therefore be roughly constant irrespective of the disc luminosity, over regions whose extension depends on the disc luminosity.

These external radiation fields provide effective seed photons for the inverse Compton scattering by relativistic electrons in the jet, and are the basis of the External Compton (EC) models for the gamma-ray production (Sikora et al. 1994, 2009). At each dis-

\* E-mail: luigi.costamante@asi.it

tance from the BH, the energy density of the different radiation components and of the magnetic field changes, as well as their ratio, which determines the IC to synchrotron luminosity ratio in the SED (the so-called ‘‘Compton dominance’’). In a leptonic framework, therefore, the location is directly connected with the gamma-ray production mechanism: for typical bulk-motion Lorentz factors  $\Gamma \gtrsim 10 - 15$ , gamma rays are mainly produced by EC on UV photons inside the BLR, by EC on IR photons between the BLR and the torus sizes, and by synchrotron self-Compton (SSC) or EC on CMB photons at further distances (Ghisellini & Tavecchio 2009; Sikora et al. 2009).

So far, EC on BLR photons (i.e. a blazar zone inside the BLR) has been the standard scenario to model the SED of the large majority of gamma-ray detected FSRQ (see e.g. Ghisellini et al. 1998; Ghisellini & Tavecchio 2008, 2009; Finke 2013, and references therein), providing a straightforward way to explain both the difference in Compton dominance and SED peak frequencies between FSRQ and BLLac objects, and the often observed fast variability (few days to few hours), indicative of compact emitting regions easier to obtain at the base of a conical jet.

However, the same external photons used for EC become targets for the  $\gamma\text{-}\gamma$  collision and pair production process. The resulting optical depths are large ( $\tau > 50$ ) on paths as short as  $10^{16}$  cm. A gamma-ray region well inside the BLR, therefore, should be accompanied by a strong cut-off in the gamma-ray spectrum above  $\sim 20$  GeV (for Ly $\alpha$  photons of ionized Hydrogen), with maximum absorption around 100-200 GeV. The densities used for the EC modeling make the BLR essentially opaque to gamma rays beyond tens of GeV. The opacity is not expected to decrease significantly even with a flat BLR geometry, elongated along the disc, instead of a spherical geometry (see e.g. Tavecchio & Ghisellini 2012). No emission at Very High Energies (VHE,  $\geq 100$  GeV) should be detectable, corresponding to the peak of the  $\gamma\text{-}\gamma$  cross section.

Nevertheless, already in the first years of operation the *Fermi* Large Area Telescope (LAT, Atwood et al. 2009) started to provide contrasting evidence, with some bright FSRQ spectra showing no sign of BLR-induced cut-offs and extending up to  $\sim 100$  GeV rest-frame energy (Costamante et al. 2010). The ‘‘smoking gun’’ of a gamma-ray region outside the BLR was provided by the detections at VHE of the FSRQ 4C+21.35 (Aleksić et al. 2011) and PKS 1510-08 (Abramowski et al. 2013; Aleksić et al. 2014). The emission measured by MAGIC in 4C+21.35 was also rapidly variable ( $t_{\text{var}} \sim 10$  minutes), indicating that very compact emitting regions of the order of  $R \sim 1.3 \times 10^{14}$  ( $\delta/10$ ) cm can exist also at pc distances from the BH, beyond the BLR (Tavecchio et al. 2011).

At the same time, possible breaks around 3-5 GeV in other objects were interpreted as evidence of  $\gamma\text{-}\gamma$  absorption on high-ionization He II line photons (Poutanen & Stern 2010). This would locate the dissipation region deep within the BLR. Oddly enough, the optical depth caused by the low-ionization Hydrogen complex – which provides the dominant contribution to the BLR optical depth, see Fig. 1 in Poutanen & Stern (2010) – was found to be rather low (a few at most), not consistent with the deep-within-BLR scenario unless assuming a very large stratification of the BLR over a wide range of distances. The re-analysis of the *Fermi* data with new data versions seems now to have reduced the evidence for such He II breaks (Stern & Poutanen 2014).

Since blazars are typically highly variable, these two apparently opposite scenarios might not be in contradiction, after all. Different states can correspond to different locations along the jet, as well as different emitting blobs. It is thus natural to expect that the observed gamma rays originate sometimes inside and sometimes

outside the BLR. This should occur most likely in FSRQ with relatively low disc luminosities, where the derived BLR size is of the same order of the expected location of the dissipation region (e.g. in internal shock scenarios, a few hundred Schwarzschild radii, see Ghisellini & Tavecchio 2009). However, this type of study has been limited so far to only a few selected objects or single outbursts.

The aim of this paper is to find out the typical behaviour of the population of bright gamma-ray FSRQ, by looking for the presence or absence of BLR-induced cut-off features in the average GeV spectra of the 100 strongest FSRQ detected by *Fermi*-LAT. This study is now made feasible by more than seven years of exposure collected by *Fermi* in survey mode as well as by the Pass 8 data, which both enhance the chance of measuring either some source counts or meaningful upper limits at the highest energies, after integrating over the whole exposure. We also take advantage of the systematic spectral study of *Fermi*-detected FSRQ in the optical by Shaw et al. (2012), which provides the luminosity of the broad emission lines for the majority of bright *Fermi* blazars.

Specifically, we want to address the following issues:

- a) if BLR absorption is a common phenomenon in *Fermi*-LAT FSRQ, and at which optical depth;
- b) if the possible absorption is consistent with the photon densities used by external Compton models;
- c) if there is a difference in location between high (flaring) and low states. That is, if the ‘‘persistent’’ (low-flux) emission is mostly produced outside the BLR and the flaring –rapidly variable– emission inside, where the cross-section of the jet is lower, or the other way round (see e.g. Bonnoli et al. 2011; Tavecchio et al. 2013; Pacciani et al. 2014; Tavani et al. 2015).

It is important to keep in mind that a cut-off in the gamma-ray spectrum at high energies does not mean *per-se* evidence of absorption due to the BLR: it can also correspond to the end of the emitting particle distribution. In such case the shape of the cut-off in the gamma-ray band depends on the shape of the cut-off in the particle distribution, as well as on the spectrum of the target photons (Lefa et al. 2012). This dependence can be used as a powerful diagnostic tool, but it is hindered by the uncertain origin of the cut-off. The focus of this paper is to test whether the LAT spectra are consistent or not with the blazar zone being inside the BLR, under the same assumptions used by EC-modeling of their SEDs.

## 2 SAMPLE SELECTION AND DATA ANALYSIS

We selected the 100 objects detected with the highest significance in the Third *Fermi*-LAT AGN catalog (3LAC, Ackermann et al. 2015), and classified as FSRQ to guarantee the presence of a BLR. The list of sources is presented in Table 1, in order of decreasing 3LAC significance. The luminosity  $L_{\text{BLR}}$  of the BLR is also reported, when available from the literature. When only the luminosity of the observed broad lines was published, for consistency we calculated  $L_{\text{BLR}}$  following Celotti et al. (1997), using the ratio of the lines to the whole BLR luminosity based on the relative weights of the lines to the Ly $\alpha$  flux in Francis et al. (1991). This is the same recipe used to calculate the BLR luminosity in all the other objects, according to the listed literature. In Table 1 we also report the corresponding BLR radius  $R_{\text{BLR}}$  and maximum optical depth  $\tau_{\text{max}}$ , defined as the optical depth at the peak of the  $\gamma\text{-}\gamma$  cross section (details in the following section). In addition to the most significant 100 FSRQ in the 3LAC, we also considered 6 further objects characterized by large values of  $L_{\text{BLR}} \geq 3 \times 10^{45}$  but still detected above  $12\sigma$  in the 3LAC.

**Table 1.** Sample of FSRQ blazars studied in this paper, sorted according to their overall significance in the 3LAC catalog (Col. 4). The upper table lists the 100 highest-significance objects in the 3LAC, while the bottom table lists the six additional objects included for their large BLR. Col. [1]: object name (from the association in the 3LAC). Col. [2]: *Fermi*-LAT name in the 3LAC. Col. [3]: redshift. Col. [4]: significance of the detection in the 3LAC (from [Ackermann et al. 2015](#)). Col. [5]: luminosity of the Broad Line Region ( $\equiv 0.1L_d$ ), in  $\text{erg s}^{-1}$ . Col. [6]: associated radius of the BLR, in cm, derived from the size-luminosity relation (see Sect. 2.1). Col. [7]: maximum optical depth, at the peak of the  $\gamma$ - $\gamma$  cross-section, for a path length  $\ell = R_{\text{BLR}}/2$  (see Sect. 2.1). Col. [8]: references for the BLR or emission lines luminosities. X14: [Xiong & Zhang \(2014\)](#) from data in [Cao & Jiang \(1999\)](#); [Chai et al. \(2012\)](#); [Liu et al. \(2006\)](#); GG10: [Ghisellini et al. \(2010\)](#); GG11: [Ghisellini et al. \(2011a\)](#); GG15: [Ghisellini & Tavecchio \(2015\)](#); I15: [Isler et al. \(2015\)](#); P14: [Pacciani et al. \(2014\)](#); S12: [Shaw et al. \(2012\)](#); Sb14: [Sbarrato et al. \(2014\)](#); T13: [Tavecchio et al. \(2013\)](#); To12: [Torrealba et al. \(2012\)](#).

Name [1]	3LAC Name [2]	$z$ [3]	$\sigma$ [4]	$L_{\text{BLR}}$ [5]	$R_{\text{BLR}}$ [6]	$\tau_{\text{BLR}}^{\text{max}}$ [7]	Refs [8]
3C 454.3	3FGL J2254.0+1608	0.859	480.74	33.3e+44	5.8e+17	55.8	GG11
4C +21.35	3FGL J1224.9+2122	0.435	219.67	16.2e+44	4.0e+17	38.9	GG11
PKS 1510-08	3FGL J1512.8-0906	0.36	207.27	7.4e+44	2.7e+17	26.3	GG11
B2 1520+31	3FGL J1522.1+3144	1.487	192.68	4.5e+44	2.1e+17	20.5	GG15
PKS 1502+106	3FGL J1504.4+1029	1.839	189.47	19.8e+44	4.4e+17	43.0	GG11
PKS 0454-234	3FGL J0457.0-2324	1.003	161.08	18.8e+44	4.3e+17	41.9	GG10
3C 279	3FGL J1256.1-0547	0.536	160.60	2.4e+44	1.5e+17	15.0	GG11
3C 273	3FGL J1229.1+0202	0.158	149.01	33.8e+44	5.8e+17	56.2	GG11
PKS 2326-502	3FGL J2329.3-4955	0.518	130.01	–	–	–	–
PKS B1424-418	3FGL J1427.9-4206	1.552	129.82	10.0e+44	3.2e+17	30.6	T13
PKS 1830-211	3FGL J1833.6-2103	2.507	129.72	–	–	–	–
4C +55.17	3FGL J0957.6+5523	0.899	112.86	3.8e+44	1.9e+17	18.7	GG11
PKS 0727-11	3FGL J0730.2-1141	1.589	111.86	–	–	–	–
4C +28.07	3FGL J0237.9+2848	1.213	105.19	18.0e+44 <sup>a</sup>	4.2e+17	41.0	I15
PKS 0402-362	3FGL J0403.9-3604	1.417	103.56	14.0e+44 <sup>a</sup>	3.7e+17	36.2	I15
Ton 599	3FGL J1159.5+2914	0.725	93.40	5.1e+44	2.3e+17	21.9	GG11
PKS 1244-255	3FGL J1246.7-2547	0.635	92.64	1.2e+44 <sup>a</sup>	1.1e+17	10.5	To12
4C +38.41	3FGL J1635.2+3809	1.814	86.97	60.0e+44	7.7e+17	74.9	GG15
PMN J2345-1555	3FGL J2345.2-1554	0.621	82.32	2.1e+44	1.4e+17	14.0	GG15
S4 0917+44	3FGL J0920.9+4442	2.19	82.11	70.8e+44	8.4e+17	81.3	GG11
PKS 2052-47	3FGL J2056.2-4714	1.491	78.95	8.5e+44 <sup>a</sup>	2.9e+17	28.1	I15
PKS 1124-186	3FGL J1127.0-1857	1.048	76.26	–	–	–	–
PKS 2142-75	3FGL J2147.3-7536	1.138	75.82	8.0e+44 <sup>a</sup>	2.8e+17	27.3	I15
B3 1343+451	3FGL J1345.6+4453	2.534	75.77	10.5e+44	3.2e+17	31.3	GG15
PKS 0805-07	3FGL J0808.2-0751	1.837	73.84	24.0e+44	4.9e+17	47.4	P14
PKS 0244-470	3FGL J0245.9-4651	1.385	73.49	27.0e+44	5.2e+17	50.2	GG15
CTA 102	3FGL J2232.5+1143	1.037	72.20	41.4e+44	6.4e+17	62.2	GG11
4C +01.02	3FGL J0108.7+0134	2.099	71.65	75.0e+44	8.7e+17	83.7	GG11
4C +14.23	3FGL J0725.2+1425	1.038	69.90	9.0e+44	3.0e+17	29.0	GG15
PKS 0250-225	3FGL J0252.8-2218	1.427	69.69	3.2e+44	1.8e+17	17.2	GG15
B2 2308+34	3FGL J2311.0+3425	1.817	66.87	–	–	–	–
B2 0716+33	3FGL J0719.3+3307	0.779	66.55	4.5e+44	2.1e+17	20.5	GG10
MG1 J123931+0443	3FGL J1239.5+0443	1.762	65.00	9.1e+44	3.0e+17	29.2	GG11
PMN J1802-3940	3FGL J1802.6-3940	1.319	63.57	15.0e+44	3.9e+17	37.4	GG15
S4 1849+67	3FGL J1849.2+6705	0.657	63.28	3.4e+44 <sup>a</sup>	1.8e+17	17.8	To12
PKS 2023-07	3FGL J2025.6-0736	1.388	63.11	22.5e+44	4.7e+17	45.8	GG10
PKS 1454-354	3FGL J1457.4-3539	1.424	62.20	45.0e+44	6.7e+17	64.8	GG10
B3 1708+433	3FGL J1709.6+4318	1.027	62.20	1.5e+44	1.2e+17	11.8	GG15
GB6 J0742+5444	3FGL J0742.6+5444	0.72	61.62	–	–	–	–
OX 169	3FGL J2143.5+1744	0.213	60.57	1.8e+44	1.3e+17	13.0	GG11
PKS 2227-08	3FGL J2229.7-0833	1.56	58.57	46.1e+44	6.8e+17	65.7	GG11
PKS 2255-282	3FGL J2258.0-2759	0.926	56.77	18.5e+44 <sup>a</sup>	4.3e+17	41.6	To12
B2 2155+31	3FGL J2157.5+3126	1.488	56.67	5.4e+44	2.3e+17	22.5	GG15
PKS 1622-253	3FGL J1625.7-2527	0.786	56.26	0.4e+44 <sup>a</sup>	6.6e+16	6.4	X14
PKS 0420-01	3FGL J0423.2-0119	0.916	56.14	7.1e+44 <sup>a</sup>	2.7e+17	25.8	X14
OC 457	3FGL J0137.0+4752	0.859	55.94	4.6e+44 <sup>a</sup>	2.1e+17	20.7	X14
PKS 2201+171	3FGL J2203.4+1725	1.076	54.14	12.0e+44	3.5e+17	33.5	GG10
OP 313	3FGL J1310.6+3222	0.997	51.97	8.4e+44	2.9e+17	28.0	GG11
TXS 0059+581	3FGL J0102.8+5825	0.644	51.50	4.5e+44	2.1e+17	20.5	GG15
S4 1030+61	3FGL J1033.8+6051	1.401	51.44	4.5e+44	2.1e+17	20.5	GG11
OG 050	3FGL J0532.7+0732	1.254	50.90	9.0e+44	3.0e+17	29.0	GG15
PKS 0440-00	3FGL J0442.6-0017	0.844	50.84	6.0e+44	2.4e+17	23.7	GG15

Table 1 – continued

Name [1]	3LAC Name [2]	$z$ [3]	$\sigma$ [4]	$L_{\text{BLR}}$ [5]	$R_{\text{BLR}}$ [6]	$\tau_{\text{BLR}}^{\text{max}}$ [7]	Refs [8]
PKS 1329-049	3FGL J1332.0-0508	2.15	49.71	67.0e+44	8.2e+17	79.1	GG11
TXS 1700+685	3FGL J1700.1+6829	0.301	49.45	–	–	–	
S4 1144+40	3FGL J1146.8+3958	1.089	48.70	11.7e+44	3.4e+17	33.1	GG11
B0218+357	3FGL J0221.1+3556	0.944	48.44	0.6e+44	7.7e+16	7.5	GG10
PKS 0215+015	3FGL J0217.8+0143	1.715	46.29	30.0e+44	5.5e+17	52.9	GG10
PKS 0336-01	3FGL J0339.5-0146	0.85	45.00	10.0e+44 <sup>a</sup>	3.2e+17	30.6	X14
4C 31.03	3FGL J0112.8+3207	0.603	44.54	–	–	–	
OM 484	3FGL J1153.4+4932	0.334	42.49	2.7e+44	1.6e+17	15.9	
TXS 1920-211	3FGL J1923.5-2104	0.874	41.03	15.0e+44	3.9e+17	37.4	GG10
MG2 J101241+2439	3FGL J1012.6+2439	1.805	40.84	13.5e+44	3.7e+17	35.5	GG15
S5 1044+71	3FGL J1048.4+7144	1.15	40.66	–	–	–	
PMN J0850-1213	3FGL J0850.2-1214	0.566	40.36	–	–	–	
PKS 0601-70	3FGL J0601.2-7036	2.409	39.57	6.0e+44	2.4e+17	23.7	GG15
B3 0650+453	3FGL J0654.4+4514	0.933	39.37	1.8e+44	1.3e+17	13.0	GG15
PKS 2320-035	3FGL J2323.5-0315	1.393	39.35	–	–	–	
PKS 0736+01	3FGL J0739.4+0137	0.18941	38.99	1.6e+44 <sup>a</sup>	1.2e+17	12.0	X14
PKS 1954-388	3FGL J1958.0-3847	0.63	37.66	1.6e+44 <sup>a</sup>	1.3e+17	12.1	X14
TXS 1206+549	3FGL J1208.7+5442	1.345	37.23	3.2e+44	1.8e+17	17.3	GG11
B2 0200+30	3FGL J0203.6+3043	0.955	36.90	0.3e+44	5.5e+16	5.3	GG15
PKS 1730-13	3FGL J1733.0-1305	0.902	36.81	6.8e+44 <sup>a</sup>	2.6e+17	25.1	X14
TXS 0106+612	3FGL J0109.8+6132	0.783	36.55	–	–	–	
PKS 0528+134	3FGL J0530.8+1330	2.07	35.90	75.0e+44	8.7e+17	83.7	GG11
PKS 0446+11	3FGL J0449.0+1121	2.153	35.64	7.2e+44	2.7e+17	25.9	GG15
B2 1732+38A	3FGL J1734.3+3858	0.976	34.65	2.0e+44	1.4e+17	13.7	GG15
PKS 0130-17	3FGL J0132.6-1655	1.02	34.58	–	–	–	
MRC 1659-621	3FGL J1703.6-6211	1.747	34.56	26.2e+44 <sup>a</sup>	5.1e+17	49.5	S12
S5 0836+71	3FGL J0841.4+7053	2.218	34.53	225.0e+44	1.5e+18	145.0	GG11
PKS 0906+01	3FGL J0909.1+0121	1.024	34.06	18.8e+44	4.3e+17	41.9	GG11
PKS 2123-463	3FGL J2126.5-4605	1.67	34.03	–	–	–	
MG2 J071354+1934	3FGL J0713.9+1933	0.54	33.61	0.6e+44	7.7e+16	7.5	GG15
PMN J1344-1723	3FGL J1344.2-1724	2.49	33.15	10.8e+44	3.3e+17	31.8	GG15
TXS 0529+483	3FGL J0533.2+4822	1.162	32.90	–	–	–	
PKS 1551+130	3FGL J1553.5+1256	1.308	32.53	15.9e+44	4.0e+17	38.5	GG11
S3 0458-02	3FGL J0501.2-0157	2.291	32.49	37.0e+44	6.1e+17	58.8	GG11
PKS B1908-201	3FGL J1911.2-2006	1.119	32.12	30.0e+44	5.5e+17	52.9	GG10
MG2 J201534+3710	3FGL J2015.6+3709	0.859	32.10	–	–	–	
CTS 0490	3FGL J2325.3-3557	0.36	32.06	–	–	–	
PKS 0451-28	3FGL J0453.2-2808	2.564	32.05	120.0e+44	1.1e+18	105.9	GG11
4C +47.44	3FGL J1637.7+4715	0.735	31.98	1.8e+44	1.3e+17	13.0	GG15
PKS 0235-618	3FGL J0236.7-6136	0.465	31.78	–	–	–	
4C +04.42	3FGL J1222.4+0414	0.966	30.02	7.2e+44	2.7e+17	25.9	GG11
PKS 0454-46	3FGL J0455.7-4617	0.858	30.01	–	–	–	
S4 1726+45	3FGL J1727.1+4531	0.717	29.92	–	–	–	
PKS 0142-278	3FGL J0145.1-2732	1.148	29.47	7.2e+44	2.7e+17	25.9	GG10
PKS 2144+092	3FGL J2147.2+0929	1.113	29.42	15.0e+44	3.9e+17	37.4	GG10
S4 1851+48	3FGL J1852.4+4856	1.25	29.34	–	–	–	
PKS 1118-05	3FGL J1121.4-0554	1.297	29.33	–	–	–	
4C +51.37	3FGL J1740.3+5211	1.381	29.27	–	–	–	
PKS 0208-512 <sup>b</sup>	3FGL J0210.7-5101	1.003	62.95 <sup>b</sup>	37e+44	6.1e+17	58.8	Sb14
TXS 0322+222	3FGL J0325.5+2223	2.066	22.18	60e+44	7.7e+17	74.9	GG15
PKS B1127-145	3FGL J1129.9-1446	1.184	22.00	112.5e+44	1.1e+18	102.5	GG10
CRATES J0303-6211	3FGL J0303.7-6211	1.348	16.76	30e+44	5.5e+17	52.9	GG15
PMN J1617-5848	3FGL J1617.4-5846	1.422	15.81	105e+44	1.0e+18	99.0	GG15
CRATES J1613+3412	3FGL J1613.8+3410	1.397	13.23	54e+44	7.3e+17	71.0	GG15

<sup>a</sup>: our calculation from the line luminosities reported in the respective reference, following [Celotti et al. \(1997\)](#).

<sup>b</sup>: this object was left out of the main FSRQ selection despite its LAT significance, because it was classified as BCU-I in the 3LAC.

The LAT data used in this paper were collected from 2008 August 5 (MJD 54683) to 2014 December 01 (MJD 56992), corresponding to approximately 7.3 years of data taking. During this time, the LAT instrument operated almost entirely in survey mode. The LAT data were analyzed following the standard procedure<sup>1</sup>, using the LAT analysis software ScienceTools v10r01p01. Only events belonging to the “Source” class (evclass=128, evtype=3) were used. We selected only events within a maximum zenith angle of 90 degrees to reduce contamination from the Earth limb gamma rays, which are produced by cosmic rays interacting with the upper atmosphere. The analysis was performed with the instrument response functions P8R2\_SOURCE\_V6 using a binned maximum likelihood method implemented in the Science tool *gllike*.

Events with energies between 0.1 and 300 GeV were extracted from an acceptance cone of 15 degrees centered at the location of the source of interest. Light curves were derived by dividing the data in bins of one week duration. The background model for the light-curve extraction included each PGWAVE source (Ciprini et al. 2007; Damiani et al. 1997) detections in each bin, to account for possible transients on short timescales that may remain below the detection threshold on timescales of years. For the spectral analysis, the background model included sources from the 3rd LAT catalog (Acero et al. 2015, hereafter 3FGL) within the ROI of 20 degrees. 3FGL sources within a radius of 10 degrees from the source of interest were left free to vary.

Each bin of the light curves and of the spectra was obtained using a power-law model for the source of interest. To derive the spectral points for the SED, the spectral parameters of background sources were fixed to the results from the fit of the complete time-integrated data. The spectral index of the source of interest was fixed to  $\Gamma = 2$  for the spectral extraction, and left free to vary for the light curve extraction. The models included the isotropic and Galactic diffuse emission components<sup>2</sup>. Both background components were left free to vary in the time integrated analysis and frozen to the average values in the SED’s bin extraction.

The gamma-ray SEDs were constructed using 4 bins per decade between 178 MeV and 300 GeV, as the best compromise between energy resolution in the cut-off region and photon statistics in each bin, for the majority of sources. We excluded the first bin (100-178 MeV) in order to reduce the chance of issues with the Galactic background, and we enlarged the last bin to increase the statistics (100-300 GeV). Each SED is then composed of 12 bins in total. When the Test Statistic (TS, Mattox et al. 1996) was  $TS < 4$  or the number of predicted photons  $N_{pred} < 3$  or the percentage error on the flux was greater than 50%, we calculated the upper limit at  $2\sigma$  confidence, using the Bayesian computation if  $TS < 1$  (Helene 1984). The statistical uncertainty on the fluxes are typically larger than the systematic uncertainty (Ackermann et al. 2012a) and only the former is considered in this paper.

## 2.1 BLR and gamma-ray spectra fitting procedure

For a wide range of ionization levels, the BLR spectrum causes an absorption feature in the gamma-ray spectrum which starts to be significant above  $\sim 20$  GeV rest-frame (see e.g. Stern & Poutanen 2014, figure 3). The spectrum below  $\sim 13$  GeV in the blazar’s rest-frame is therefore essentially unabsorbed, and can thus be taken as representation of the intrinsic source spectrum interacting with the

Hydrogen-induced radiation of the BLR ( $\text{Ly}\alpha$  emission and continuum). The presence or absence of a possible BLR absorption feature can thus be determined by comparing the extrapolation of the spectral fit performed in the unabsorbed part of the spectrum with the actual observed data at the highest energies. This corresponds to a “best-case scenario” for BLR absorption, that is without considering possible intrinsic cut-offs (and excluding ad-hoc fine-tuned additional emission pile-ups in the spectrum).

To model the effects of  $\gamma$ - $\gamma$  absorption, we adopted the same assumptions and values used for the SED modeling with the External Compton process on BLR photons (Ghisellini & Tavecchio 2009; Sikora et al. 2009). Namely, we assume that the BLR intercepts and reprocesses about 10% of the disc luminosity into an isotropic radiation field with uniform energy density  $U_{\text{BLR}}$  and radius  $R_{\text{BLR}}$  from the BH. Following Tavecchio & Ghisellini (2008) and in part the double-absorber approximation in Poutanen & Stern (2010), we approximate the BLR spectrum with a Planckian spectrum peaked at 10.2 eV (corresponding to a temperature of  $\sim 42000$  K) renormalized to match the BLR energy density. This provides a good approximation to the Hydrogen  $\text{Ly}\alpha$  emission and recombination continuum complex which provides the strongest contribution to the BLR gamma-ray opacity (Poutanen & Stern 2010). The actual BLR spectrum contains typically many lines and recombination continua, but their effect is generally smeared out by the broadness of the  $\gamma$ - $\gamma$  cross section and the averaging over angles. The precise shape of the absorption feature depends also on the ionization state of the gas, but its main effects can be well approximated by an absorption feature peaking around 100-200 GeV (see Stern & Poutanen 2014, figure 3). Note that for our study it is irrelevant if a break in the spectrum below 10 GeV is due to high-ionization He II lines or is intrinsic: our focus is on the interaction with the low-ionization, Hydrogen-based part of the BLR emission, since it is the one typically used for EC models (yielding the largest energy density) and it is unavoidable in any scenario inside the BLR, even more so if within the smaller high-ionization radius of the BLR. The normalization of the Planckian spectrum is obtained by imposing that its integrated energy density  $U$  is equal to  $U_{\text{BLR}}$ , where

$$U_{\text{BLR}} = \frac{L_{\text{BLR}}}{4\pi R_{\text{BLR}}^2 c} \quad R_{\text{diss}} < R_{\text{BLR}} \quad (1)$$

$R_{\text{diss}}$  is the distance from the BH of the dissipation region in the jet producing the gamma-rays. The actual shape of the BLR spectrum longward of this peak (which might be significantly broader than the blackbody approximation if the illuminating spectrum is a multicolor black-body, see e.g. Tavecchio & Ghisellini 2008) is not important in our case, since it affects photons at energies above  $\sim 100$  GeV. Assuming the scaling relation  $R_{\text{BLR}} = 10^{17} L_{\text{d},45}^{1/2}$  cm (Ghisellini & Tavecchio 2009; Sikora et al. 2009), the energy density inside the BLR is constant at  $U_{\text{BLR}} \simeq 0.22 \text{ erg cm}^{-3}$ .

In this framework, the only free parameter determining the optical depth  $\tau(E)$  is the path length of the gamma rays inside the BLR sphere, from the production region (at  $R_{\text{diss}}$  from the black hole) to the border of the BLR, at  $R_{\text{BLR}}$ . We thus parameterized the absorption in terms of path length  $\ell$ , in units of  $10^{16}$  cm. The BLR luminosity changes the optical depth by determining the size of the BLR (and thus the photon path). The spectral shape of the absorption feature is determined by the convolution of the Planckian approximation with the  $\gamma$ - $\gamma$  cross section averaged over angles for an isotropic field (Aharonian 2004). The corresponding maximum optical depth  $\tau_{\text{max}}(E)$  is reached at  $E \simeq 110$  GeV. For each value of the path  $\ell$ , therefore, there is a corresponding value of  $\tau_{\text{max}}$ .

<sup>1</sup> <http://fermi.gsfc.nasa.gov/ssc/data/analysis/>

<sup>2</sup> iso\_P8R2\_SOURCE\_V6\_v06.txt and gll\_iem\_v06.fits

**Table 2.** Results of the BLR absorption fits to the gamma-ray SED data. Col. [1]: object Name. Col. [2]: redshift. Col. [3]: number of data points above 20 GeV rest-frame. It indicates how much farther the spectrum extends into the “forbidden region” of strong BLR absorption. Col. [4]: average restframe energy, in GeV, of the last “good” datapoint in the spectrum at high energy (see text). Col. [5]: best fit model of the data below 13 GeV rest-frame (namely, with the lowest  $\chi_r^2$ ). It is the model used to extrapolate the spectrum to estimate the optical depth. Col. [6]: path length  $\ell$  inside the BLR, in units of  $10^{16}$  cm. Obtained by extrapolating the model in Col. 5 to the full band. Col. [7]: corresponding maximum optical depth, at the peak of the  $\gamma$ - $\gamma$  cross-section with a Planckian spectrum. Col. [8]: maximum optical depth assuming the dissipation region is located at  $R_{\text{diss}} = \max(2 \times 10^{16} \text{ cm}, R_{\text{BLR}}/2)$ . Col. [9]: corresponding path length inside the BLR, in units of  $10^{16}$  cm, to be compared with Col. 6; Col. [10]: logarithm of the ratio between the observed data flux of the highest-energy data point and the expected model with  $\tau_{\text{BLR}}^{\text{max}}$ . It gives the separation in the SED (in orders of magnitudes) between the observed and expected fluxes if the assumptions of the EC(BLR) model were right. Col. [11]: probability value (from F-test) between the model with free (measured) or fixed ( $\ell_{\text{BLR}}$ ) paths inside the BLR (see text). A 3- $\sigma$  exclusion corresponds to a p-value  $\leq 2.7\text{e-}03$ . Col. [12], [13]: path and corresponding  $\tau_{\text{F}}^{\text{max}}$  for the fit with a logparabolic model plus BLR absorption allowing all parameters to be free. Col. [14]: model of the fullband LAT spectrum yielding the lowest  $\chi_r^2$ , among: logparabola (logp), logparabola with free BLR absorption (logptau), power-law with under-exponential cutoff at high energy with  $\beta_c = 1/3$  (exp03). See Sect. 2.1. Col. [15]: flag indicating if the upper limit is below the last “good” datapoint in the SED, i.e. if it is meaningful to constrain the spectral steepening (strong) or not. If it is, the fits are checked that they comply to the UL constraints.

Name [1]	$z$ [2]	n>20 [3]	MaxBin [4]	best<13 [5]	Path [6]	$\tau^{\text{max}}$ [7]	$\tau_{\text{BLR}}^{\text{max}}$ [8]	Path <sub>BLR</sub> [9]	ratio [10]	p-value(BLR) [11]	Path <sub>F</sub> [12]	$\tau_{\text{F}}^{\text{max}}$ [13]	bestfitFull [14]	UL [15]
3C 454.3	0.859	3	77.3	logp	0.63±0.09	1.23	55.8	28.9	21.0	5.8e-10	0.60±0.13	1.15	exp03	strong
4C +21.35	0.435	2	59.7	logp	0.16±0.11	0.31	38.9	20.1	12.8	1.9e-07	0.16±0.17	0.31	exp03	strong
PKS 1510-08	0.36	3	100.6	logp	0.00±0.16	0.00	26.3	13.6	11.2	3.3e-07	0.00±0.21	0.00	logp	no
B2 1520+31	1.487	2	58.2	logp	0.17±0.13	0.33	20.5	10.6	6.3	9.7e-07	0.21±0.23	0.40	exp03	no
PKS 1502+106	1.839	3	66.4	logp	0.37±0.11	0.72	43.0	22.2	14.9	2.6e-07	0.42±0.23	0.81	exp03	strong
PKS 0454-234	1.003	3	83.3	logp	0.20±0.13	0.40	41.9	21.7	16.0	1.0e-07	0.25±0.22	0.48	exp03	no
3C 279	0.536	3	63.9	logp	0.36±0.16	0.69	15.0	7.7	4.8	1.7e-06	0.32±0.25	0.62	logptau	no
3C 273	0.158	0	15.2	logp	0.00±0.47	0.00	56.2	29.1	1.1	7.8e-05	0.00±0.67	0.00	logp	strong
PKS 2326-502	0.518	1	35.5	logp	0.88±0.17	1.69	–	–	–	–	0.96±0.25	1.85	logptau	strong
PKS B1424-418	1.552	3	106.1	logp	0.37±0.08	0.71	30.6	15.8	12.6	1.4e-08	0.35±0.18	0.68	exp03	strong
PKS 1830-211	2.507	3	82.0	logp	0.48±0.09	0.92	–	–	–	–	0.24±0.15	0.47	exp03	strong
4C +55.17	0.899	4	140.5	logp	0.04±0.07	0.08	18.7	9.7	8.0	9.0e-09	0.09±0.16	0.17	exp03	no
PKS 0727-11	1.589	2	60.6	logp	0.29±0.10	0.56	–	–	–	–	0.34±0.23	0.66	exp03	strong
4C +28.07	1.213	2	51.8	logp	0.00±0.15	0.00	41.0	21.2	12.1	6.5e-07	0.00±0.21	0.00	logp	strong
PKS 0402-362	1.417	0	17.9	logp	0.11±0.44	0.21	36.2	18.7	1.3	1.0e-03	0.24±0.73	0.46	logp	strong
Ton 599	0.725	3	71.7	logp	0.00±0.35	0.00	21.9	11.3	8.1	9.6e-05	0.00±0.49	0.00	logp	no
PKS 1244-255	0.635	2	38.2	logp	0.14±0.21	0.27	10.5	5.5	2.0	3.0e-06	0.21±0.33	0.40	logp	no
4C +38.41	1.814	3	65.8	logp	0.44±0.17	0.84	74.9	38.7	25.5	7.3e-08	0.46±0.27	0.88	exp03	no
PMN J2345-1555	0.621	3	67.4	logp	0.31±0.11	0.60	14.0	7.2	4.7	1.8e-07	0.28±0.20	0.54	exp03	no
S4 0917+44	2.19	2	42.0	logp	0.46±0.13	0.89	81.3	42.1	18.3	1.9e-06	0.25±0.25	0.47	exp03	strong
PKS 2052-47	1.491	2	58.3	logp	0.00±0.31	0.00	28.1	14.6	9.5	7.4e-05	0.00±0.47	0.00	logp	no
PKS 1124-186	1.048	3	85.2	logp	0.00±0.07	0.00	–	–	–	–	0.00±0.16	0.00	logp	no
PKS 2142-75	1.138	1	28.1	logp	0.54±0.08	1.05	27.3	14.1	3.1	5.1e-08	0.65±0.13	1.25	logptau	strong
B3 1343+451	2.534	4	147.0	logp	0.17±0.04	0.34	31.3	16.2	13.3	2.2e-10	0.19±0.11	0.37	exp03	no
PKS 0805-07	1.837	3	66.4	logp	0.24±0.10	0.45	47.4	24.5	16.4	4.7e-07	0.37±0.25	0.72	exp03	strong
PKS 0244-470	1.385	1	31.4	logp	0.29±0.16	0.57	50.2	26.0	7.1	1.7e-05	0.21±0.29	0.41	exp03	strong
CTA 102	1.037	2	47.6	logp	0.26±0.29	0.50	62.2	32.2	16.2	1.3e-05	0.18±0.45	0.34	logp	no
4C +01.02	2.099	3	72.5	logp	0.32±0.18	0.61	83.7	43.3	30.5	6.0e-07	0.17±0.35	0.34	logp	no
4C +14.23	1.038	2	47.7	logp	0.00±0.12	0.00	29.0	15.0	7.9	2.0e-06	0.13±0.21	0.25	exp03	strong
PKS 0250-225	1.427	2	56.8	logp	0.02±0.15	0.05	17.2	8.9	5.3	1.3e-06	0.02±0.27	0.04	logp	no
B2 2308+34	1.817	3	65.9	logp	0.10±0.16	0.19	–	–	–	–	0.28±0.30	0.54	logp	no
B2 0716+33	0.779	2	41.6	logp	0.56±0.09	1.07	20.5	10.6	4.4	1.9e-08	0.59±0.16	1.15	exp03	no
MG1 J123931+0443	1.762	3	64.6	logp	1.22±0.14	2.37	29.2	15.1	9.6	9.5e-06	1.25±0.24	2.42	logptau	no
PMN J1802-3940	1.319	2	54.2	logp	0.24±0.30	0.46	37.4	19.4	11.0	3.7e-05	0.21±0.59	0.40	logp	no
S4 1849+67	0.657	2	38.8	logp	0.38±0.09	0.74	17.8	9.2	3.4	3.9e-06	0.43±0.14	0.83	logp	no
PKS 2023-07	1.388	2	55.9	logp	0.00±0.24	0.00	45.8	23.7	14.4	2.2e-05	0.00±0.40	0.00	logp	no

Table 2 – continued

Name [1]	$z$ [2]	$n>20$ [3]	MaxBin [4]	best<13 [5]	Path [6]	$\tau^{max}$ [7]	$\tau_{BLR}^{max}$ [8]	Path <sub>BLR</sub> [9]	ratio [10]	p-value(BLR) [11]	Path <sub>F</sub> [12]	$\tau_F^{max}$ [13]	bestfitFull [14]	UL [15]
PKS 1454-354	1.424	2	56.7	logp	0.41±0.27	0.80	64.8	33.5	20.0	1.4e-05	0.47±0.49	0.91	logp	no
B3 1708+433	1.027	2	47.4	logp	0.00±0.54	0.00	11.8	6.1	3.6	3.0e-03	0.00±0.79	0.00	logp	no
GB6 J0742+5444	0.72	2	40.2	logp	0.00±0.50	0.00	–	–	–	–	0.00±0.79	0.00	logp	no
OX 169	0.213	1	28.4	logp	0.00±0.81	0.00	13.0	6.7	1.8	1.8e-03	0.00±1.16	0.00	logp	no
PKS 2227-08	1.56	0	18.9	logp	0.00±0.26	0.00	65.7	34.0	2.6	7.7e-05	0.05±0.45	0.09	logp	strong
PKS 2255-282	0.926	1	25.3	logp	0.00±0.99	0.00	41.6	21.5	3.8	2.4e-03	0.00±1.63	0.00	logp	no
B2 2155+31	1.488	2	58.2	logp	0.79±0.20	1.52	22.5	11.6	6.9	9.6e-05	0.90±0.35	1.74	exp03	no
PKS 1622-253	0.786	2	41.8	logp	0.37±0.20	0.72	6.4	3.3	1.3	7.6e-05	0.49±0.33	0.95	logp	no
PKS 0420-01	0.916	2	44.8	logp	0.00±0.43	0.00	25.8	13.3	6.5	1.8e-04	0.00±0.70	0.00	logp	no
OC 457	0.859	2	43.5	logp	0.13±0.13	0.24	20.7	10.7	4.9	4.9e-08	0.23±0.22	0.45	exp03	no
PKS 2201+171	1.076	2	48.6	logp	0.00±0.81	0.00	33.5	17.3	9.4	1.1e-03	0.00±1.07	0.00	logp	no
OP 313	0.997	3	83.1	pow	0.69±0.23	1.34	28.0	14.5	10.7	8.9e-05	0.30±0.32	0.58	exp03	no
TXS 0059+581	0.644	2	38.5	logp	0.00±0.88	0.00	20.5	10.6	4.2	3.1e-03	0.00±1.39	0.00	logp	no
S4 1030+61	1.401	2	56.2	logp	0.44±0.11	0.84	20.5	10.6	6.1	8.1e-08	0.32±0.20	0.62	exp03	no
OG 050	1.254	2	52.7	logp	0.00±0.18	0.00	29.0	15.0	8.6	1.4e-05	0.08±0.30	0.16	logp	strong
PKS 0440-00	0.844	2	43.1	logp	1.08±0.30	2.08	23.7	12.2	5.4	9.6e-04	0.84±0.45	1.63	exp03	no
PKS 1329-049	2.15	3	73.7	logp	0.00±0.42	0.00	79.1	40.9	29.7	3.4e-04	0.00±0.70	0.00	logp	no
TXS 1700+685	0.301	1	30.4	logp	0.38±0.75	0.74	–	–	–	–	0.04±1.07	0.08	logp	no
S4 1144+40	1.089	3	86.9	logp	0.00±0.22	0.00	33.1	17.1	13.6	8.8e-06	0.00±0.32	0.00	logp	no
B0218+357	0.944	3	80.9	logp	0.03±0.20	0.07	7.5	3.9	2.7	2.0e-04	0.00±0.37	0.00	logp	no
PKS 0215+015	1.715	3	63.5	pow	0.92±0.23	1.78	52.9	27.4	17.2	8.9e-06	0.59±0.41	1.13	exp03	no
PKS 0336-01	0.85	2	43.3	logp	0.20±0.42	0.38	30.6	15.8	7.2	5.6e-04	0.35±0.70	0.68	logp	no
4C 31.03	0.603	2	37.5	logp	1.95±1.04	3.77	–	–	–	–	1.56±1.52	3.01	logp	no
OM 484	0.334	0	17.5	pow	7.46±1.76	14.42	15.9	8.2	0.0	6.1e-01	7.35±2.69	14.20	exp03	no
TXS 1920-211	0.874	1	24.6	logp	0.72±0.32	1.39	37.4	19.4	3.1	7.8e-04	1.09±0.63	2.10	logptau	strong
MG2 J101241+2439	1.805	1	20.7	pow	1.82±0.44	3.52	35.5	18.4	1.7	3.7e-03	2.11±0.94	4.07	logptau	strong
S5 1044+71	1.15	2	50.3	logp	0.16±0.12	0.30	–	–	–	–	0.28±0.19	0.55	exp03	no
PMN J0850-1213	0.566	2	36.6	logp	0.00±0.81	0.00	–	–	–	–	0.00±1.17	0.00	logp	no
PKS 0601-70	2.409	2	44.8	logp	0.00±1.06	0.00	23.7	12.2	6.3	4.2e-03	0.00±1.72	0.00	logp	no
B3 0650+453	0.933	2	45.2	logp	0.00±0.91	0.00	13.0	6.7	3.6	8.5e-03	0.00±0.82	0.00	logp	no
PKS 2320-035	1.393	1	31.5	pow	0.94±0.21	1.82	–	–	–	–	0.82±0.41	1.59	logptau	strong
PKS 0736+01	0.18941	1	27.8	logp	0.00±1.14	0.00	12.0	6.2	1.4	5.1e-02	0.00±1.74	0.00	logp	no
PKS 1954-388	0.63	1	21.4	logp	1.21±0.28	2.34	12.1	6.3	0.6	1.6e-03	1.25±0.51	2.42	logptau	strong
TXS 1206+549	1.345	0	17.3	pow	2.10±0.55	4.07	17.3	9.0	0.3	1.5e-02	1.43±1.01	2.77	logptau	strong
B2 0200+30	0.955	2	45.7	logp	0.00±0.27	0.00	5.3	2.7	1.5	9.3e-05	0.07±0.46	0.14	logp	no
PKS 1730-13	0.902	2	44.5	logp	0.22±0.08	0.43	25.1	13.0	6.0	8.9e-09	0.28±0.14	0.54	exp03	no
TXS 0106+612	0.783	0	13.2	logp	3.40±9.70	6.58	–	–	–	–	3.52±16.50	6.80	logp	no
PKS 0528+134	2.07	0	12.8	logp	2.22±1.08	4.30	83.7	43.3	0.7	3.5e-03	2.21±2.29	4.27	exp03	strong
PKS 0446+11	2.153	2	41.5	logp	0.00±0.30	0.00	25.9	13.4	5.9	1.2e-05	0.00±0.54	0.00	logp	no
B2 1732+38A	0.976	1	26.0	logp	0.00±0.31	0.00	13.7	7.1	1.4	3.4e-06	0.00±0.42	0.00	exp03	no
PKS 0130-17	1.02	1	26.6	logp	0.00±2.35	0.00	–	–	–	–	0.00±3.53	0.00	logp	no
MRC 1659-621	1.75	1	20.3	logp	3.33±1.35	6.44	49.5	25.6	2.1	9.6e-03	3.47±2.57	6.72	exp03	no
S5 0836+71	2.218	1	23.8	logp	0.00±2.70	0.00	145.0	75.0	11.6	2.7e-02	0.00±4.34	0.00	logp	no
PKS 0906+01	1.024	1	26.6	logp	0.00±0.78	0.00	41.9	21.7	4.4	8.8e-05	0.00±1.22	0.00	logp	no

Table 2 – continued

Name [1]	$z$ [2]	$n>20$ [3]	MaxBin [4]	best<13 [5]	Path [6]	$\tau^{max}$ [7]	$\tau_{BLR}^{max}$ [8]	PathBLR [9]	ratio [10]	p-value(BLR) [11]	Path <sub>F</sub> [12]	$\tau_F^{max}$ [13]	bestfitFull [14]	UL [15]
PKS 2123-463	1.67	0	19.7	pow	3.69±2.08	7.13	–	–	–	–	2.47±3.67	4.77	exp03	no
MG2 J071354+1934	0.54	0	11.4	logp	3.50±1.48	6.77	7.5	3.9	0.2	8.1e-01	3.38±2.80	6.53	exp03	strong
PMN J1344-1723	2.49	3	81.6	pow	0.68±0.36	1.31	31.8	16.4	11.7	1.3e-03	0.00±0.71	0.00	exp03	no
TXS 0529+483	1.162	1	28.4	logp	0.00±0.31	0.00	–	–	–	–	0.00±0.59	0.00	logp	strong
PKS 1551+130	1.308	1	30.4	pow	0.32±0.86	0.61	38.5	19.9	5.1	3.3e-03	0.00±1.62	0.00	exp03	no
S3 0458-02	2.291	2	43.3	logp	0.00±0.11	0.00	58.8	30.4	14.0	4.2e-07	0.00±0.23	0.00	logp	strong
PKS B1908-201	1.119	1	27.9	logp	0.09±0.12	0.17	52.9	27.4	6.0	1.6e-06	0.04±0.25	0.07	logp	strong
MG2 J201534+3710	0.859	2	43.5	logp	0.00±0.16	0.00	–	–	–	–	0.00±0.22	0.00	logp	strong
CTS 0490	0.36	0	10.1	logp	1.10±1.44	2.13	–	–	–	–	1.14±2.66	2.21	logp	strong
PKS 0451-28	2.564	0	14.8	logp	2.99±0.74	5.77	105.9	54.8	1.4	4.2e-03	2.80±1.56	5.41	logptau	strong
4C +47.44	0.735	1	22.8	logp	0.00±1.45	0.00	13.0	6.7	1.1	3.2e-03	0.00±2.30	0.00	exp03	no
PKS 0235-618	0.465	0	10.8	pow	2.63±2.12	5.09	–	–	–	–	0.14±3.94	0.27	logp	strong
4C +04.42	0.966	0	14.5	logp	0.00±6.57	0.00	25.9	13.4	0.6	1.1e-01	0.00±10.33	0.00	logp	no
PKS 0454-46	0.858	1	24.4	logp	0.00±1.94	0.00	–	–	–	–	0.00±3.02	0.00	logp	no
S4 1726+45	0.717	0	12.7	logp	0.00±1.22	0.00	–	–	–	–	0.00±2.01	0.00	logp	strong
PKS 0142-278	1.148	0	15.9	logp	0.00±9.78	0.00	25.9	13.4	0.7	1.5e-01	0.00±15.76	0.00	logp	no
PKS 2144+092	1.113	0	15.6	logp	2.12±3.50	4.11	37.4	19.4	0.6	3.6e-02	2.24±6.07	4.32	logp	no
S4 1851+48	1.25	1	29.6	logp	0.00±0.62	0.00	–	–	–	–	0.00±0.97	0.00	logp	strong
PKS 1118-05	1.297	0	17.0	logp	0.00±0.71	0.00	–	–	–	–	0.00±1.25	0.00	logp	strong
4C +51.37	1.381	2	55.7	logp	0.00±0.51	0.00	–	–	–	–	0.00±0.84	0.00	logp	no
PKS 0208-512	1.003	1	26.3	logp	0.76±0.30	1.47	58.8	30.4	5.8	1.8e-03	0.86±0.54	1.67	exp03	strong
TXS 0322+222	2.066	0	12.8	pow	2.97±1.00	5.75	74.9	38.7	0.4	1.2e-01	3.10±2.17	5.98	exp03	strong
PKS B1127-145	1.184	0	16.2	logp	0.00±3.44	0.00	102.5	53.0	2.3	1.5e-02	0.00±6.00	0.00	logptau	no
CRATES J0303-6211	1.348	0	17.4	pow	4.18±2.84	8.09	52.9	27.4	1.3	3.4e-02	1.09±5.18	2.10	logp	no
PMN J1617-5848	1.422	0	17.9	pow	0.00±3.47	0.00	99.0	51.2	3.2	5.0e-02	0.20±8.00	0.39	exp03	no
CRATES J1613+3412	1.397	1	31.5	logp	0.00±2.87	0.00	71.0	36.7	11.0	4.2e-02	0.00±4.43	0.00	logp	no

The fitting procedure was performed in two steps: first we fitted the data in the unabsorbed part of the LAT spectrum (up to 13 GeV rest-frame) with both a powerlaw and a log-parabolic model, choosing the best model as the one with the lowest  $\chi_r^2$ . In the second step, we extrapolated this model to the whole LAT band (typically one decade further in energy) and fitted the optical depth  $\tau(E) = \ell \tau_{16}(E)$  to the data (where  $\tau_{16}(E)$  is the optical depth for a path of  $10^{16}$  cm), keeping fixed the spectral parameters to the unabsorbed values. In addition, we fitted the log-parabolic model plus BLR absorption leaving all parameters free, to check the robustness of the  $\ell$  values when all parameters could be optimized at the same time.

The resulting photon path  $\ell$  and optical depth  $\tau_{\max}$  are to be compared with the values for an emitting region deep inside the BLR,  $\ell_{\text{BLR}}$  and  $\tau_{\max}^{\text{BLR}}$ . As benchmark for such case, we assumed that  $R_{\text{diss}}$  is located at  $R_{\text{BLR}}/2$  (i.e. halfway between the BH and the BLR), with a lower limit of  $2 \times 10^{16}$  cm (the lowest value reported in Ghisellini et al. 2010). Therefore  $\tau_{\max}^{\text{BLR}}$  is the optical depth corresponding to a photon path  $\ell_{\text{BLR}} = R_{\text{BLR}} - R_{\text{diss}}$ .

Our procedure gives the best-fit values of the photon path  $\ell$  inside the BLR under the assumption that the intrinsic gamma-ray spectrum at higher energies follows the same shape measured in the unabsorbed range. This does not mean that the assumed intrinsic model plus absorption provides the best fit to the data: it simply gives the largest possible optical depth allowed by the LAT data in the best-case scenario of no intrinsic cut-off in the spectrum. To check for alternative scenarios with *no* BLR absorption, we also fitted the full-band LAT data with a pure log-parabolic model and with a power-law model with a high-energy cut-off, of the form:

$$\frac{dN}{dE} = N_0 E^{-\Gamma} \exp\left(-\left(\frac{E}{E_c}\right)^{\beta_c}\right) \quad (2)$$

where the exponent  $\beta_c$  regulates the strength of the cut-off: super-exponential if  $\beta_c > 1$  and under-exponential if  $\beta_c < 1$ . The importance of the shape of the spectrum in the cut-off region is determined by its direct connection with the shape of the underlying particle distribution and the spectrum of the seed-photon field: in general an exponential cut-off in the particle spectrum generates an under-exponential cut-off in the emitted gamma-ray spectrum, in the Thomson regime (Lefa et al. 2012). To limit the number of free parameters, we have kept  $\beta_c$  fixed at  $\beta_c = 1/3$ , corresponding to an electron spectrum with exponential cut-off interacting with synchrotron photons (see Lefa et al. 2012, table 1).

The whole procedure was implemented in a python script, and the fit was performed on the gamma-ray SED data using the routines in NumPy (curvefit and lmfit). This procedure is not as accurate as a direct maximum likelihood fit to the LAT event data, but it is much faster and from our tests it gives comparable results within the errors. A disadvantage is that it does not make full use of the upper limit information in the fit, but in no case of our sample does it play a decisive role in the fit results. Given the larger systematic uncertainties brought by the still limited knowledge of the BLR itself (in geometry, extension and spectrum), and the possible accommodation of small differences with slight changes in the position of the emitting region, we do not deem a more detailed analysis necessary for the scope of our population study.

### 3 RESULTS: AVERAGE SPECTRA

We first fitted the average spectrum integrated over the whole exposure time. Table 2 lists the results of the BLR absorption fits. The model spectral parameters and the comparison with non-absorption scenarios are reported in the Appendix (Table A1), together with the gamma-ray SED of each single source and the corresponding fitting models (Fig. A1).

Table 2 provides also the following information: a) the ratio (in logarithm) between the observed flux of the highest-energy data point and the expected flux assuming a location deep inside the BLR; i.e. how many orders of magnitude the observed LAT flux is above the expected flux from deep within the BLR; b) the p-value of the F-test between the model with free (measured) or fixed (at  $\ell_{\text{BLR}}$ ) BLR absorption, using the same intrinsic model determined in the unabsorbed band. This gives the probability of measuring the path value  $\ell$  if the null-hypothesis  $\ell = \ell_{\text{BLR}}$  (i.e. deep within the BLR) were true.

For the large majority of sources, there is no evidence for strong BLR absorption (e.g.  $\tau_{\max} \gtrsim 10$ ). In 83% of the objects, the LAT spectrum extends well beyond 20 GeV, in the “forbidden zone” according to the BLR photon densities. The possible photon path  $\ell$  inside the BLR is constrained to be  $\ell < 3 \times 10^{16}$  cm in 95% of the objects, with an average  $\tau_{\max} \simeq 0.74$  and a path length of  $\ell_{\text{avg}} \simeq 0.38 \times 10^{16}$  cm. That is comparable with the typical sizes of the gamma-ray emitting region used in SED modeling. Even considering the small sub-sample of objects with  $\ell > 3 \times 10^{16}$  cm (6% of the total), the average photon path is still  $\ell_{\text{avg}} \simeq 4.3 \times 10^{16}$  cm, with a corresponding  $\tau_{\max} \simeq 8.3$ , significantly less than expected from the deep-within-BLR scenario.

The same trend emerges considering the additional sample of 6 sources characterized by large BLRs: three of them are not compatible with strong BLR absorption, while for the other three the data are not really constraining. For these, some BLR absorption – though slightly lower than assumed for  $\tau_{\text{BLR}}$  – might be compatible (see Appendix, Fig. A2). Remarkably, in none of the 106 objects considered here BLR absorption is strictly required: all the LAT spectra can be fitted equally well (or better) by models with no BLR absorption.

Figure 1 shows a comparison between the expected and measured optical depths for all the objects with an estimate of the BLR luminosity (83 among 106 objects in total). The optical depths compatible with the LAT data are much smaller than expected, by 1.5 to 2 orders of magnitude, with 73% of the objects having  $\tau_{\max} < 1$ , and 88% less than 3. Of the total sample of 106 objects, only 8 FSRQ ( $\sim 8\%$ ) have  $\tau_{\max} > 5$ .

In summary, considering all 106 Fermi-LAT FSRQ of our sample, only approximately *one out of ten* seems compatible with significant absorption, either for lack of constraints at higher energies (flux too low) or for having an estimate of  $\tau_{\max} > 5$ . The maximum optical depth  $\tau_{\max}$  is less than 1 in 73% of the total sample, and less than 3 in 87% of the cases. This means that, in general, for about 2/3 of the objects the LAT data do not seem consistent with any BLR absorption, and for the remaining 1/3 the data are compatible at most with a very low optical depth. Even in such case, however, the smooth cut-offs are equally or better reproduced with intrinsic models, either a log-parabolic shape or an intrinsic, under-exponential cut-off at high-energy.

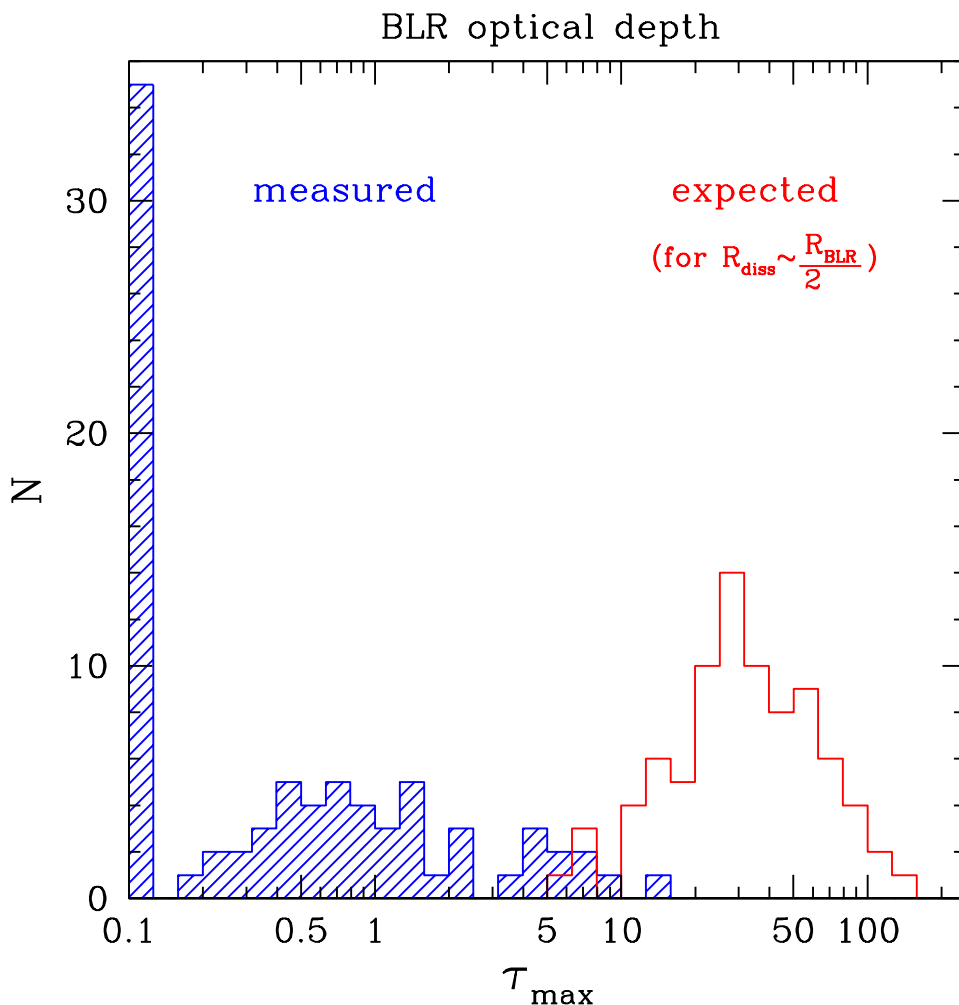


**Figure 1.** Histogram of the distribution of the possible (as measured) vs expected maximum optical depths  $\tau_{\max}$  (i.e. at the peak of the  $\gamma$ - $\gamma$  cross-section, see text), for the 83 objects for which  $L_{\text{BLR}}$  is available. Histograms are calculated with 10 bins per decade, in logarithmic space. Where  $\tau_{\max} \leq 0.1$ , objects are counted in the first bin. The optical depths measured with the fits can be considered upper limits to the possible amount of BLR absorption. The LAT data indicate that the possible optical depth due to BLR photons is at most a factor  $\sim 30 - 100\times$  lower than typically used in EC(BLR) models, and it is less than 1 in about 2/3 of the sample.

#### 4 RESULTS: HIGH VS LOW STATES

For 21 objects with the highest overall statistics and/or a lightcurve characterized by clearly recognizable flares of high brightness (on a 7-days time bin), we divided the spectra in a “high” and “low” state by making a specific cut in flux or epoch, adapted to each source’s lightcurve. The results of the fits are reported in Table 3, together with the cut value for each source. Lightcurves and flux cuts are shown in the Appendix, Fig. A3, together with the corresponding gamma-ray spectra on the side.

With the exception of 3C 273, for which the high/low data are not really constraining, all objects show absent or very low BLR absorption in *both* high and low states. This means that, on average, the emitting region in these sources seems located outside the BLR most of the time, regardless of variability. Changes by a factor of 2 in the limiting flux do not affect the results. There seems to be no relevant difference between the two states, with the possible exception of three cases where the attenuation seems slightly stronger during the high state than in the low state (4C +28+07, PKS 0454-234 and PKS 2326-502). This might indicate an emitting region closer to the BLR during flares, but it could also be caused by a

different cut-off in the emitting particle spectrum. Given that the allowed absorption even in such cases is rather low, with  $\tau_{\max} \sim 2 - 4$  and photon paths  $\ell \sim 1 - 2 \times 10^{16}$  cm, the latter seems a more likely scenario.

##### 4.1 VHE-detected FSRQ

A particularly interesting case is represented by the FSRQ 4C +21.35 and PKS 1510-08. Their detection at VHE by MAGIC (Aleksić et al. 2011) and H.E.S.S. (Abramowski et al. 2013) provided evidence for an emitting region beyond the BLR, also in objects with strong BLR and IR emission. This is confirmed by the LAT data, with spectra in the high state extending to  $\sim 80$  GeV rest-frame with no signs of cut-off (see Fig. 2).

Remarkably, we find that also during the low states the LAT spectrum extends to very high energies – almost  $\sim 100$  GeV – with no sign of BLR absorption. This means that for both 4C +21.35 and PKS 1510-08, the dominant gamma-ray emitting region is *always* located beyond the BLR, and not only during the high, VHE-bright and fast-flaring episodes. The lack of any indication of high-energy cut-off in the spectrum does not leave much room for  $\gamma$ - $\gamma$  absorp-

**Table 3.** Results of the BLR absorption fits to separate “High” and “Low” states, for a sub-sample of FSRQs. The division of the data is done with a cut in flux or epoch (see Fig. 2 and Fig. A3). Col. [1]: object name. Col. [2]: state of the source, as defined in Col. 3. Col. [3]: flux  $N_{cut}$  (in  $\text{cm}^{-2} \text{s}^{-1}$ ) or time interval separating the High from Low-state spectra. Namely, the High (Low) datasets are obtained summing all intervals in the 7-day lightcurve with  $\text{Flux} \geq N_{cut}$  ( $< N_{cut}$ ), or the intervals specified by MJD. Col. [4]: number of data points above 20 GeV rest-frame. Col. [5]: average rest-frame energy, in GeV, of the last “good” datapoint in the spectrum at high energy (namely with  $\text{TS} > 4$  and  $\text{npred} > 3$  and flux error  $< 50\%$ , see Sect. 2); Col. [6]: best fit model of the data below 13 GeV rest-frame (i.e. with the lowest  $\chi_r^2$ ). It is the model used to extrapolate the spectrum to estimate the optical depth. Col. [7]: path length inside the BLR, in units of  $10^{16}$  cm, obtained by extrapolating the model in Col. 6 to the full LAT band. Col. [8]: corresponding maximum optical depth, at the peak of the  $\gamma$ - $\gamma$  cross-section (see text). Col. [9]: model of the fullband LAT spectrum yielding the lowest overall  $\chi_r^2$ , among: logparabola (logp), logparabola with BLR absorption (logptau) or power-law with under-exponential cutoff with  $\beta_c = 1/3$  (exp03). Col. [10]: flag indicating if the upper limit in the SED is below the last “good” datapoint at high energy, i.e. if it is meaningful to constrain the spectral steepening (strong) or not.

Name [1]	State [2]	Cut [3]	n>20 [4]	MaxBin [5]	best<13 [6]	Path [7]	$\tau^{max}$ [8]	bestfitFull [9]	UL [10]
3C 273	High	1.0e-6	0	11.2	logp	0.16±0.37	0.31	logp	strong
	Low		0	11.2	logp	0.0±11.7	0.00	exp03	no
3C 279	High	0.9e-6	2	61.7	logp	0.20±0.21	0.38	logp	no
	Low		2	61.7	logp	0.27±0.11	0.52	exp03	strong
4C +14.23	High	0.6e-6	1	40.2	logp	0.00±0.99	0.00	logp	no
	Low		1	40.2	logp	0.24±0.16	0.46	exp03	strong
4C +21.35	High	1.0e-6	2	57.6	logp	0.07±0.10	0.14	logptau	strong
	Low		2	57.6	logp	0.24±0.15	0.47	exp03	strong
4C +28.07	High	0.5e-6	1	21.5	logp	0.72±0.26	1.40	exp03	strong
	Low		2	43.7	logp	0.00±0.15	0.00	exp03	strong
4C +38.41	High	0.5e-6	2	55.6	logp	0.34±0.14	0.65	logptau	strong
	Low		1	27.3	logp	0.84±0.11	1.62	logptau	strong
B0218+357	High	0.5e-6	1	38.4	logp	0.03±0.16	0.05	logp	no
	Low		3	158.8	pow	0.03±0.17	0.07	exp03	no
CTA 102	High	0.9e-6	1	40.2	logp	0.53±0.07	1.02	logptau	strong
	Low		0	19.8	logp	0.86±0.43	1.67	exp03	strong
MG1 J123931+0443	High	0.4e-6	1	26.8	logp	0.76±0.16	1.47	logptau	strong
	Low		2	54.5	logp	0.16±0.17	0.31	logp	no
PKS 0402-362	High	0.5e-6	1	23.5	logp	0.00±0.58	0.00	exp03	no
	Low		1	23.5	logp	0.51±0.53	0.98	exp03	no
PKS 0440-00	High	mjd <sup>a</sup>	1	36.4	pow	0.59±0.23	1.14	exp03	no
	Low		0	17.9	logp	1.71±1.09	3.30	logp	no
PKS 0454-234	High	0.5e-6	1	39.6	logp	0.36±0.18	0.69	logptau	strong
	Low		2	80.4	logp	0.20±0.08	0.38	logptau	no
PKS 0727-11	High	mjd <sup>b</sup>	3	104.0	logp	0.00±0.10	0.00	exp03	no
	Low		2	51.1	pow	0.81±0.16	1.56	exp03	strong
PKS 1329-049	High	0.6e-6	1	30.6	logp	0.93±1.13	1.79	exp03	no
	Low		2	62.2	logp	0.96±0.67	1.86	exp03	no
PKS 1502+106	High	0.65e-6	3	114.0	logp	0.28±0.09	0.54	logptau	no
	Low		2	56.1	logp	0.00±0.21	0.00	logp	no
PKS 1510-08	High	1.7e-6	2	54.6	logp	0.00±0.19	0.00	logp	no
	Low		3	111.1	logp	0.00±0.31	0.00	logp	no
PKS 1830-211	High	mjd <sup>c</sup>	2	69.3	logp	0.60±0.09	1.16	exp03	strong
	Low		2	69.3	logp	0.00±0.08	0.00	logp	strong
PKS 2326-502	High	0.8e-6	0	14.7	logp	2.17±0.73	4.20	exp03	strong
	Low		1	30.0	logp	0.32±0.14	0.62	logptau	strong
PKS B1424-418	High	1.0e-6	3	102.5	logp	0.33±0.12	0.63	exp03	strong
	Low		3	102.5	logp	0.58±0.13	1.12	logptau	strong
S5 1044+71	High	0.5e-6	1	20.9	logp	0.19±0.24	0.36	exp03	strong
	Low		2	42.5	logp	0.14±0.12	0.27	logptau	strong

a: MJD 54960–55000 and 56460–56545

b: MJD  $\geq 55740$

c: MJD 55130–55221, 55452–55592 and 56054–56180

tion by other radiation fields as well, like soft photons from other parts of the jet, at least in the UV-optical range. Adopting an EC scenario, the LAT data indicate therefore that the seed photons should be provided by the infrared torus and not by the BLR.

However, even in this case the EC scenario might face some problems. IR photons are targets for  $\gamma$ - $\gamma$  collisions as well, this time with TeV photons. The expected optical depth from the torus

radiation is again large, and should start to be important already around  $\sim 500$  GeV rest-frame, reaching the maximum from 1 TeV onward (e.g. Protheroe & Biermann 1997; Donea & Protheroe 2003). Given the strong thermal IR emission in these two sources (Malmrose et al. 2011), the EC(IR) scenario predicts a strong cut-off in the VHE spectrum above 500 GeV rest-frame, which is already reached by the MAGIC spectrum in the case of 4C +21.35.

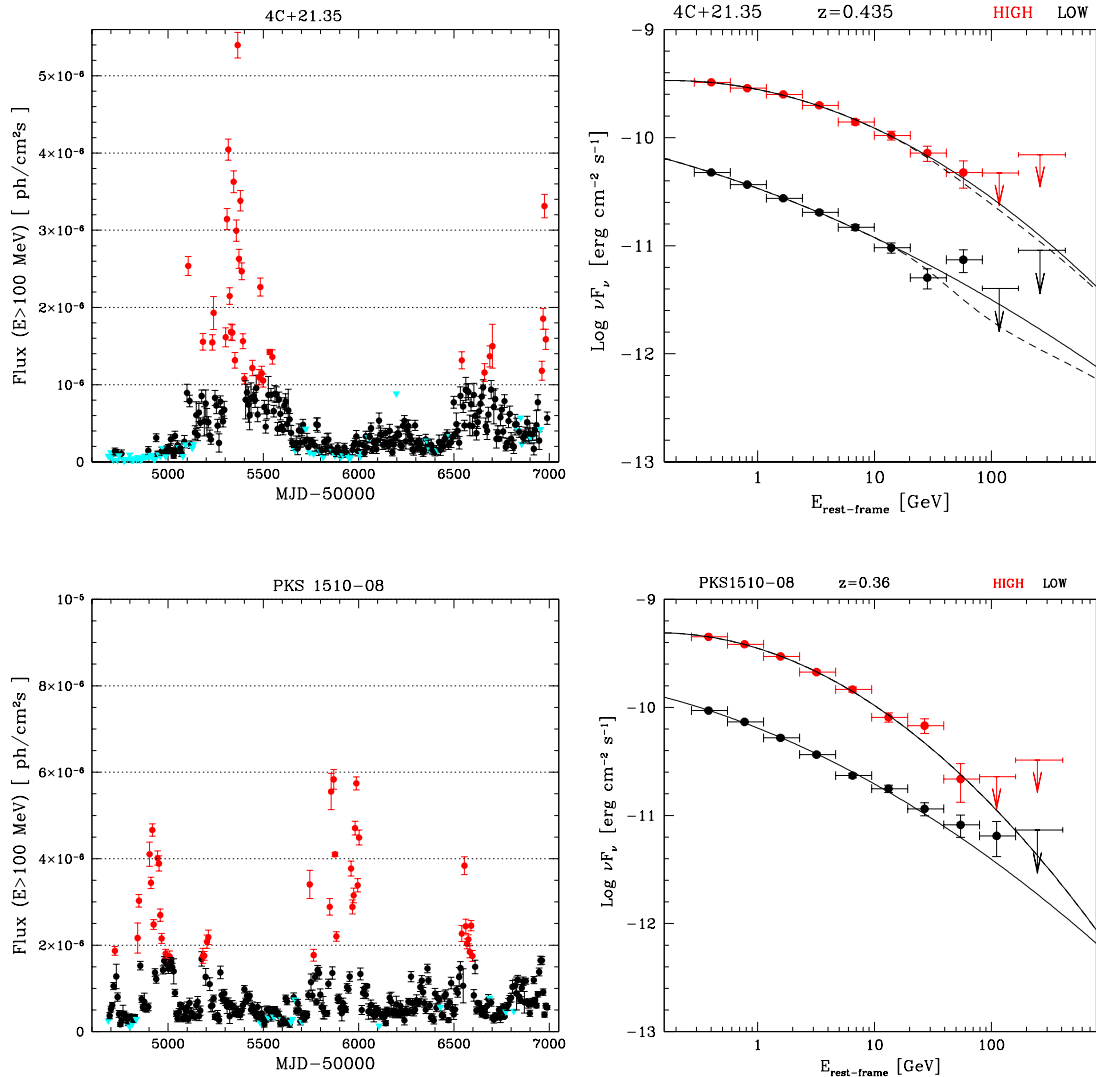


**Figure 2.** Lightcurves and spectra of the TeV-detected FSRQ 4C+21.35 and PKS 1510-08, divided in High (red) and Low (black) states. Upper limits are at the  $2\sigma$  level (see text).

If future observations were to detect emission well beyond 500 GeV with no cut-off after correction for EBL absorption, it will mean that the gamma-ray region is located even beyond the torus inner radius, at tens of parsecs from the central engine, where the VLBA core is often located (e.g. Pushkarev & Kovalev 2012) and where the jet becomes transparent to millimeter wavelengths (Marscher 2012; Sikora et al. 2008).

It remains a puzzle to explain very fast gamma-ray variability (implying very compact regions) at pc distances from the BH, which has been observed also in PKS 1510-08 at GeV energies (see e.g. Abdo et al. 2010; Saito et al. 2013; Brown 2013), with flux-doubling timescales as short as  $\sim 20$  min (Foschini et al. 2013).

#### 4.2 The case of 3C 454.3

Since the launch of *AGILE* and *Fermi*, 3C 454.3 has been one of the brightest sources in the gamma-ray sky (Vercellone et al. 2009; Abdo et al. 2009). It is also one of the most violently vari-

able blazars, with flux variations of several order of magnitude and observed down to shortest timescales allowed by photon statistics (sub-hour, see Abdo et al. 2011). With strong and variable broad emission lines (Isler et al. 2013; León-Tavares et al. 2013), for a BLR luminosity  $L_{\text{BLR}} \sim 2 - 5 \times 10^{45} \text{ erg s}^{-1}$  and  $R_{\text{BLR}} \sim 6 \times 10^{17} \text{ cm}$ , 3C 454.3 is one of the prototypical FSRQ-type blazars.

Its SED has been commonly modeled with EC on BLR photons (Ghisellini & Tavecchio 2009; Abdo et al. 2009; Bonnoli et al. 2011), but specific outbursts have been explained in several alternative ways: with EC on IR photons from the torus (for example the huge flare of year 2005, though no gamma-ray telescope was in operation at that epoch, Sikora et al. 2008) or with IC on radiation from clouds beyond the BLR reflecting the jet emission itself (“mirror models”, see Vittorini et al. 2014, and refs therein), with SSC emission outside the BLR (Pian et al. 2006) and also as the result of star-jet interaction (Khargulyan et al. 2013). The fact that the dissipation zone can move outside the BLR during single flares has been generally supported by the detection of several photons

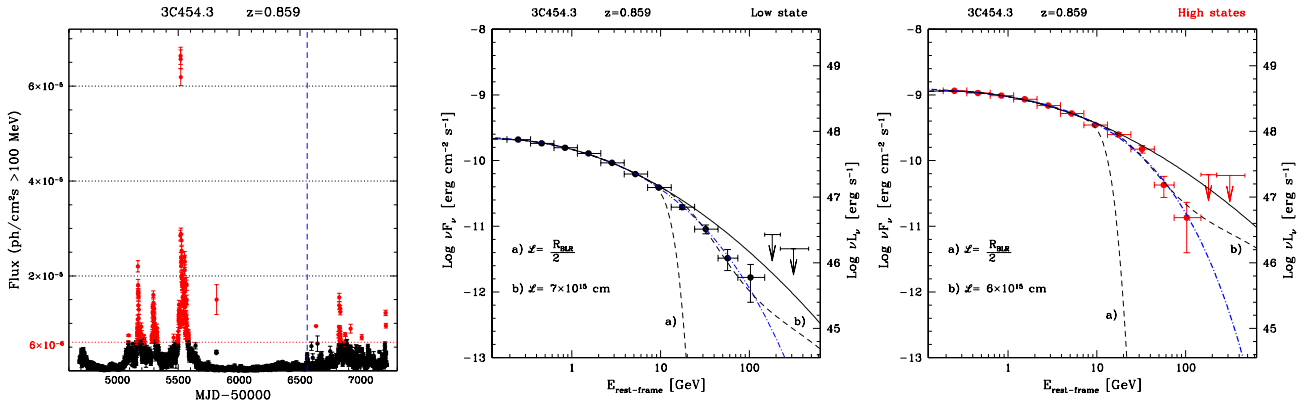


**Figure 3.** Left: lightcurve of 3C 454.3 in 1-day bins, from the automatic quick-look analysis of the LAT monitored bright source list. This lightcurve is used only to show the chosen cuts, with different colors if the bin belongs to the “High” (in red) or “Low” (black) flux state. The dividing line chosen for the extraction of the spectra is  $6 \times 10^{-6} \text{ cm}^{-2} \text{ s}^{-1}$ . The blue dashed line marks the epoch of the  $\sim 13$ -hr flare reported in Pacciani et al. (2014) as “Period A”, whose spectrum is shown in Fig. 4. Center and Right: SED of the Low and High states, at rest-frame energies. In both cases the spectrum extends up to  $\sim 100$  GeV, with no sign of strong BLR cut-off. Full lines correspond to the best fit of the spectrum below 13 GeV. Dashed lines correspond to the BLR-absorbed spectrum, with two different path lengths inside the BLR: a) assuming the emitting region is deep within the BLR (at  $R_{\text{BLR}}/2$ ), and b) at the value from the best fit of the spectrum ( $7$  and  $6 \times 10^{15}$  cm). The blue dot-dashed line shows how a power-law model with under-exponential high-energy cut-off ( $\beta_c = 1/3$ ), corresponding to an intrinsic cut-off in the particle distribution with emission in the Thomson regime (Lefa et al. 2012), can provide an excellent fit, reproducing all the properties of the LAT spectra (see text).

above 20 GeV (Abdo et al. 2011; Britto et al. 2016) and by the hard spectrum with no steepening (Pacciani et al. 2014).

Our analysis of the average gamma-ray spectrum confirms an emitting region beyond the BLR in high state. Remarkably, it reveals that the spectrum extends with a smooth shape up to  $\sim 100$  GeV rest-frame also in the low state, with a slight steepening beyond 30 GeV which leaves room only for a small amount of possible  $\gamma\text{-}\gamma$  absorption (see Fig. 3). The allowed photon path inside the BLR is only  $\ell = (0.74 \pm 0.28)$  and  $(0.55 \pm 0.17) \times 10^{16}$  cm, for low and high states respectively, corresponding to a  $\tau_{\text{max}} = 1.4$  and 1.1. These values are incompatible with a dissipation region well within the BLR.

The shape of the spectrum, however, is better reproduced by a power-law model with under-exponential cut-off rather than the log-parabolic model with free BLR absorption (see Fig. 3,  $\chi_r^2 \simeq 1.3$  vs  $2.4 - 4.0$ ). With  $\beta_c \equiv 1/3$  (see Eq. 2), the model fits the gamma-ray spectrum very well with a photon index  $\Gamma = 1.83 \pm 0.02$  and  $E_{\text{cut-off}} = 0.14 \pm 0.02$  GeV for the low state, and  $\Gamma = 1.82 \pm 0.02$  with  $E_{\text{cut-off}} = 0.30 \pm 0.05$  GeV for the high state. Together, these two results (spectrum extending to 100 GeV and better fitted without BLR absorption) indicate that the steepening seen in 3C 454.3 is most likely intrinsic, related to the end of the emitting particle distribution rather than due to  $\gamma\text{-}\gamma$  interactions with BLR photons.

If this scenario is correct, we can expect that under the right acceleration conditions 3C 454.3 could become a strong VHE emitter and detectable by present air-Cherenkov telescopes. Indeed this seems to have been the case during a relatively low-flux flare of 3C 454.3 in 2009, reported by Pacciani et al. (2014). During a 13-hours timespan (“period A” in Pacciani et al. 2014, marked by the dashed line in Fig. 3), the gamma-ray spectrum was hard (power-law photon index  $\Gamma < 2$ ), namely rising with energy in the SED. We have re-analyzed this flare with Pass 8 data (using in this case an unbinned maximum likelihood fit to the LAT event data, given the low counts) and can confirm the result, obtaining  $\Gamma = 1.8 \pm 0.1$ . This means that 3C 454.3 in that circumstance was behaving like

an high-energy-peaked BL Lac object (HBL), with the gamma-ray emission in the SED peaking around or above 100 GeV (Fig. 4).

Given the flux measured by *Fermi*-LAT and the emission beyond the BLR, Fig. 4 shows that 3C 454.3 can be easily detected at VHE in less than an hour with the present generation of air-Cherenkov telescopes, and up to 300-400 GeV despite the large redshift and EBL attenuation. This makes 3C 454.3 an excellent and important target for VHE observations during such flares, which can reveal the spectral evolution of the freshly accelerated particles near the cut-off region (Lefa et al. 2012; Romoli et al. 2017).

## 5 DISCUSSION

The *Fermi*-LAT spectra indicate that for 2/3 of our FSRQ sample there is no evidence of BLR absorption ( $\tau_{\text{max}} < 1$ ), while for the remaining 1/3 of the objects the possible optical depths are a factor 30-100 $\times$  lower than expected in EC(BLR) models.

To keep a low optical depth consistent with a gamma-ray emitting region well inside the BLR, one can envisage two possibilities: 1) to decrease the photon densities by enlarging the size of the BLR, or 2) to shift the  $\gamma\text{-}\gamma$  threshold at higher energies by selecting preferred angles of interaction.

In the first case, since the optical depth  $\tau \propto 1/R_{\text{BLR}}$ , a factor 100 $\times$  less in  $\tau$  means that the size of the BLR should be 100 $\times$  larger than it appears from reverberation mapping, in fact close to the torus location. This is much larger than the scatter on the reverberation mapping relation (2 vs 0.13 dex, e.g. Bentz et al. 2013). However, this size would imply that the energy density  $U_{\text{BLR}}$  available for the external Compton process is lower as well, and by a factor  $10^{-4}$  given that  $U_{\text{BLR}} \propto L_d R_{\text{BLR}}^{-2}$ . Such low values would make the EC process highly inefficient, requiring a much larger jet power to compensate, and would put the energy density of BLR photons well below the other local energy densities in the jet comoving frame (Ghisellini & Tavecchio 2009; Sikora et al. 2009). These arguments hold also considering a wide stratification of the BLR (e.g.

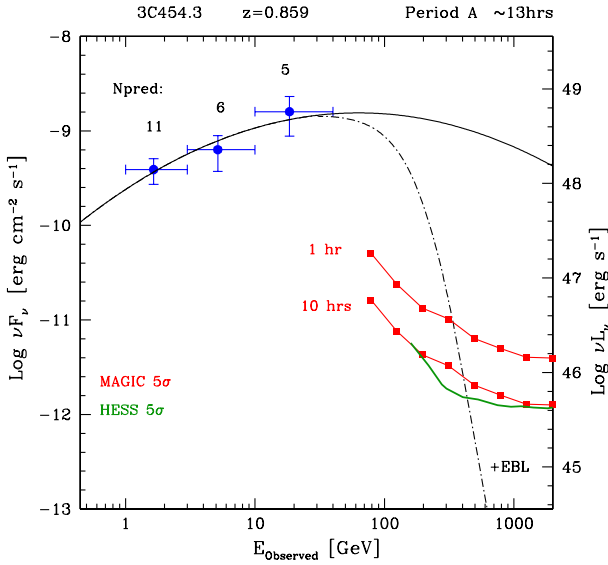


**Figure 4.** SED of 3C454.3 during the flare defined “Period A” in Pacciani et al. (2014), re-analyzed with Pass 8 data. The number of predicted source photons in each bin is also shown. We note that here the spectrum is plotted in the *observed energy scale* (not at rest-frame), for easier comparison with sensitivity curves. The spectrum is hard ( $\Gamma = 1.8 \pm 0.1$ ), as typical in *Fermi*-detected HBLs but not FSRQ. This locates the gamma-ray peak in the SED at or above 100 GeV, with consequently copious emission at VHE. As example, we show an hypothetical log-parabolic spectrum (with curvature parameter  $\beta = 0.25$ ) normalized to the LAT flux, assuming that the SED peak is around 100 GeV (full line). The  $5\sigma$  sensitivity curves for 10 and 1 hour of observations with MAGIC in stereo mode (Aleksić et al. 2016) are also plotted, together with the 10-hour curve for the present H.E.S.S. performance for the 4-telescope array (Holler et al. 2015). After accounting for EBL absorption using Domínguez et al. 2011 (dot dashed line), the sensitivity curves show that 3C454.3 can be easily detected up to  $\sim 3$ –400 GeV during such flares.

Abolmasov & Poutanen 2017), in the only scenario that could reduce the opacity with respect to our estimates. Namely, if the bulk of the BLR emissivity were produced much further out with respect to the radius from reverberation mapping or photoionization methods, which should correspond to the virial radius of the BLR clouds (see e.g. Negrete et al. 2013). Stratification due to higher-ionization lines instead develops towards inner radii, and thus does not impact our results (see Sect. 2.1).

In the second case, one can assume that the BLR is actually flattened onto the accretion disc, such that the interaction of the jet gamma rays with BLR photons occurs preferentially at low angles (Lei & Wang 2014; Abolmasov & Poutanen 2017). To push the BLR absorption feature –starting at  $\sim 20$  GeV in the isotropic case– outside the observed data, for example at 100 GeV rest-frame, one needs an average shift of  $\sim 5\times$  of the energy threshold. Since the latter is given by

$$E_{\text{thr}} = \frac{2m_e^2 c^4}{(1 - \mu)\epsilon} \quad (3)$$

where  $\epsilon$  is the energy of the target photon,  $\mu = \cos\theta$  and  $\theta$  is the collision angle, a back-of-the-envelope estimate shows that the typical angle between gamma rays and target photons should be less than 30 deg. This would reduce again the efficiency of the EC mechanism, due to the similar kinematics of the interaction. In any

case, it would locate the emitting region again very far from the BH and beyond the BLR radius (typically by more than a factor  $\sqrt{3}$  larger), in order to achieve such small interaction angles.

Both alternative scenarios do not seem able to keep the external Compton on BLR UV photons as a viable mechanism to produce the gamma-ray emission in FSRQ. When the LAT data allow for possible BLR absorption (in only 1/3 of the objects), the low optical depths indicate that, if indeed inside the BLR, the location of the dissipation region must be close to the BLR radius given by reverberation mapping ( $R_{\text{diss}} \approx R_{\text{BLR}}$ ), probably between the inner and outer borders of a more realistic representation of the BLR (e.g. Böttcher & Els 2016). In these conditions, also the isotropic assumption for  $\gamma$ – $\gamma$  absorption is not valid anymore, and the actual values of  $\tau$  will strongly depend on the details of the (yet uncertain) geometry of the BLR in relation to the size of the dissipation region (see e.g. Finke 2016). In any case, the low optical depths imply that also the EC cooling on BLR photons is depressed, under the same conditions.

However, the same data are equally and often better reproduced by a spectrum with intrinsic curvature and no BLR absorption. In addition, with these fits there is no relevant difference in properties and parameters values among objects with (1/3) or without (2/3) possible mild absorption. The inside-BLR scenario would instead require a dichotomy in jet parameters, given the very different energy of the main seed photons for IC, in the two cases (UV or IR). While not definitive, therefore, the simplest explanation is that also in these objects the emission occurs mostly outside the BLR.

This leads to the conclusion that for the large majority of FSRQ (94%) and/or for most of the time, the gamma-ray emission is produced outside the BLR, and not by IC scattering of BLR photons.

This conclusion has two important consequences. First, it means that the steepening often seen in the LAT gamma-ray spectra at higher energies is intrinsic, and not due to interaction with the environment. The shape of the cut-off depends on both the electron distribution and the target photon field, as well as the regime of the interaction (Thomson or Klein-Nishina). This dependence has been studied by Lefa et al. (2012) and provides a powerful diagnostic tool for the acceleration and cooling mechanisms in the jet, especially if coupled with the knowledge of the synchrotron cut-off (see also Romoli et al. 2017). Indeed the gradual steepening seen in the majority of our sample seems to favour a SSC scenario or an EC on IR photons, both in the Thomson regime, with the parameter  $\beta_e$  regulating the cut-off of the electron distribution between 2 and 1, depending on the importance of the synchrotron losses in the acceleration scenario.

The second consequence is an apparent discrepancy: if there is no interaction of the jet’s electrons and photons with the BLR, why the observed strong correlation between the gamma-ray luminosity and the broad line emission (Sbarato et al. 2012)? Such correlation suggests a tight jet-disc connection, between jet power (traced by gamma-ray luminosity) and accretion rate and disc luminosity (traced by the BLR luminosity with BH mass estimates), with the transition between radiatively efficient and inefficient accretion discs occurring at  $L_d/L_{\text{Edd}} \sim 10^{-2}$  (Sbarato et al. 2014). Our result suggests that the BLR acts as a proxy for the accretion regime and the disc luminosity, but does not affect directly the gamma-ray luminosity through more efficient cooling. In other words, jets seem born that way: the division between FSRQ and BLLacs seems determined by the conditions of accretion (if radiatively efficient or inefficient, and by the accretion rate) rather than the environment and location of the dissipation region, inside or

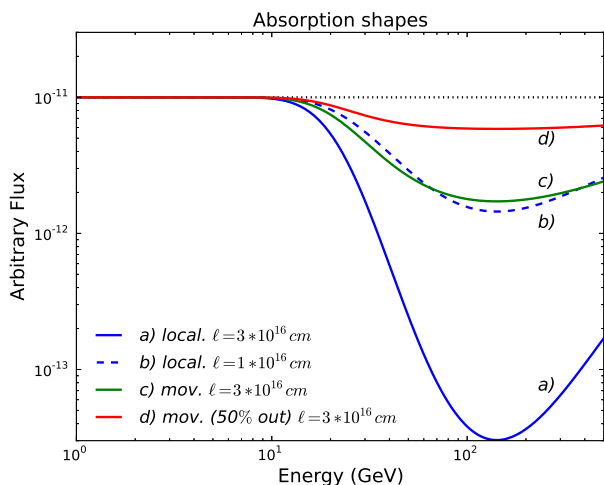


**Figure 5.** Absorption shapes for different emission scenarios: *a)* localized emission, with the same path  $\ell$  for all photons ( $e^{-\tau}$  absorption); *b)* same as *a)* but closer to  $R_{\text{BLR}}$  (path  $\ell = 1 \times 10^{16}$  cm vs  $3 \times 10^{16}$  cm); *c)* constant emission from moving blob fully inside the BLR, up to  $R_{\text{BLR}}$  (Eq. 4); *d)* constant emission from moving blob, with 50% of the flux coming from outside the BLR. Scenarios *c)* and *d)* present shallower attenuation features than scenario *a)*, for the same overall path  $\ell$  inside the BLR. This translates to the possibility of slightly longer paths inside the BLR for approximately the same absorption shape (compare lines *b)* with *c)*).

outside the BLR. Alternatively, the role of the BLR is simply taken by the IR emission from the torus. In such case the BLR would act as a proxy for the torus emission, via the disc luminosity.

We note that our values for the possible optical depths are consistent with those reported in [Stern & Poutanen \(2014\)](#), after accounting for the different scaling (since they scale the optical depth to the Thomson cross section, their values must be divided by  $\approx 5$  to be compared with ours). However we arrive to the opposite interpretation considering the much larger sample, with the majority of FSRQ without BLR absorption, the extension of the spectra at high energies without clear breaks, the very low optical depths inconsistent with EC models and the better fits with intrinsic models.

### 5.1 Caveats

Our result comes with two important caveats. One concerns the long integration time of the spectra, needed by the extremely low countrates at high energy. In principle, there is the possibility that a series of short hard flares occurring beyond the BLR might provide all the detected high-energy photons, while for most of the time the emission is actually inside the BLR. This could skew the fit, simulating the effects of a lower absorption in the averaging process. It seems unlikely because flares should be frequent, short and not too strong in order to remain below the flux threshold of the high/low-state separation, for nearly all sources in our sample. Unfortunately the limited collection area of the LAT detector ( $\sim 1 \text{ m}^2$ ) cannot provide a definitive answer to this issue. Such answer could be provided by future imaging air-Cherenkov arrays like CTA ([Actis et al. 2011](#); [Acharya et al. 2013](#)), thanks to their huge collection areas and lower energy threshold. The optimum would be represented by the proposed “5@5” array ([Aharonian et al. 2001](#)), with a threshold as low as 5 GeV. A low threshold below 10 GeV is necessary to get a handle also on the unabsorbed part of the gamma-ray spectrum.

The second caveat concerns the kinematics of the emission. Our assumption is that the bulk of the emission originates on average at roughly the same location inside the BLR. For example, from a preferred dissipation region within the jet (e.g. a standing shock) at a given distance from the central engine. In this case the produced gamma rays travel the same path  $\ell$  inside the BLR, and thus have all the same probability of survival  $e^{-\tau(E,\ell)}$ . The time-integrated spectrum is therefore attenuated by  $e^{-\tau(E,\ell)}$ . This is the absorption factor commonly used in the literature for BLR absorption.

Instead, if we assume that the observed flux is dominated by the emission of a single relativistic blob over a relatively long time, the actual distance traveled by the blob in that timeframe can be quite large, because of the shortening of the arrival times due to the Doppler effect. Gamma rays originate from different locations inside the BLR, and the net absorption effect can be different. The travel  $\Delta R$  of a blob with velocity  $\beta c$  in an observed time interval  $\Delta t_{\text{obs}}$  is  $\Delta R \simeq \Delta t_{\text{obs}} * \beta c / (1 - \beta \cos(\theta))$ . For a blazar jet seen at an angle  $\theta \simeq 1/\Gamma$ , for which  $\cos(\theta) = \beta$ ,  $\Delta R \simeq \Delta t_{\text{obs}} * \beta c * \Gamma^2$ . With bulk Lorentz factors  $\Gamma \geq 10$ , an observed emission time of  $\geq 10^5$  s can correspond to a travel of the emitting region  $\Delta R \geq 10^{17}$  cm, i.e. from deep within the BLR to its borders or beyond. In such a case, the last part of the emission is less affected by BLR attenuation than the first part, since the actual photon path inside the BLR becomes shorter and shorter. The resulting attenuation shape on the total integrated spectrum becomes shallower than exponential (see Fig. 5), and this could relax the constraints on the path inside the BLR.

For example, assuming that all the blob emission takes place inside the BLR but up to the BLR border (the most favourable scenario for EC on BLR), the flux becomes attenuated as

$$N(E) \propto E^{-\Gamma} \frac{(1 - e^{-\tau(E,\ell)})}{\tau(E,\ell)} \quad (4)$$

which goes as  $\tau^{-1}$  for large values of  $\tau$ . Here  $\ell$  corresponds to the path inside the BLR since the start of the blob emission.

However, this possibility does not change the main outcome of our study. Fitting all sources with the shape of Eq. 4, the limits on the path length inside the BLR increase only mildly, by a factor 2–3. The maximum possible path inside the BLR is still limited to small values ( $\ell < 3 \times 10^{16}$  cm) for 86% of the total sample of 106 objects (compared to the 94% of the  $e^{-\tau}$  attenuation shape). We can conclude that also in this scenario the gamma-ray emission seems produced outside the BLR for most of the sources. This scenario however does allow for significantly larger  $\tau$  in about 10% of the FSRQ, for which  $\tau_{\text{max}} \geq 10$  with an average maximum path  $\ell_{\text{avg}} \simeq 9 \times 10^{16}$  cm. Future observations with Cherenkov arrays in the 10–300 GeV range should provide more detailed answers, thanks to the much larger collection area at high energies. Interestingly, if the blob path during the emission were to continue beyond the BLR, the time-integrated spectral shape could have a step depending on the percentage of the blob emitting time passed inside or outside the BLR (see Fig. 5), and this could become a diagnostic tool with CTA.

## 6 CONCLUSIONS

We have analyzed 7.3 years of LAT data to study the spectra of 106 FSRQ characterized by the largest gamma-ray photon statistics and/or the largest BLR luminosities and sizes, looking for evidence of  $\gamma$ - $\gamma$  absorption on the Hydrogen-based BLR emission.

The result is that, for the large majority of *Fermi* blazars (9 out of 10), there is NO evidence of strong interaction of the jet gamma rays with BLR photons. The emission seems to originate *almost always* outside the BLR, both on average and during high/flaring or low-flux states. To this respect there is no relevant difference between high/flaring states and low states. The percentage of objects where the LAT spectrum is consistent with a relatively strong BLR absorption is limited to only a few % of the FSRQ population (at maximum 10%, depending on the emission scenario). The implications are remarkable and far-reaching.

(i) External Compton on BLR photons is disfavoured as main mechanism for the gamma-ray emission in *Fermi* FSRQ. This conclusion holds also in the alternative scenario of a BLR much larger ( $100\times$ ) than given by reverberation mapping, requiring  $10\times$  higher bulk motion Lorentz factors of the plasma to reach an equivalent energy density in the jet frame. A higher Lorentz factor would increase the energy density of the other external photons as well. A viable alternative for the EC mechanism is provided by the IR photons from the dusty torus (Sikora et al. 2009).

(ii) The gamma-ray spectrum measured by *Fermi*-LAT is mostly intrinsic, up to energies where  $\gamma$ - $\gamma$  absorption by the EBL or IR radiation from the torus kicks in. The mild, smooth cut-off often seen between few GeV to few tens GeV is most likely due to the end of the accelerated particle distribution. This opens up the possibility of powerful diagnostics on the accelerated particle spectrum, studying the shape of the cut-off and in comparison with the synchrotron spectrum (Lefa et al. 2012; Romoli et al. 2017).

(iii) Without suppression by the BLR, the gamma-ray emission in FSRQ can reach the VHE band with potentially very high luminosities, as demonstrated by the flares of 3C 454.3. Therefore also FSRQ can be good targets for VHE telescopes: they can be easily detected by present and future air-Cherenkov arrays even at high redshift (around or beyond  $z \sim 1$ ), up to 300–400 GeV, thanks to the very high photon fluxes and the low intensity of the EBL (Aharonian et al. 2006; Ackermann et al. 2012b).

If indeed gamma rays originate mostly outside the BLR, our result indicates that the VHE sky with CTA should be much richer of FSRQ than previously expected.

Given the strong correlation observed between gamma-ray luminosity and BLR emission in *Fermi* blazars (Sbarrato et al. 2014), our result suggests that the BLR acts as a proxy of the accretion properties but does not affect directly the jet emission through cooling. The classical distinction between FSRQ and BL Lacs becomes thus somewhat fuzzier: differences like high/low-peaked SEDs and Compton dominance cannot be attributed to the cooling on BLR photons and their high energy density. This result may have implications also for the interpretation of the “blazar sequence” (Ghisellini et al. 1998, 2017), since the jet physical parameters derived from the SED modeling change depending on the emission mechanism and dominant seed photons. A general re-assessment of the blazar emission parameters and re-modeling of their SED (with external Compton on IR photons, SSC or with  $100\times$  lower  $U_{\text{BLR}}$ ) seems in order.

## ACKNOWLEDGEMENTS

We thank the anonymous referee for the helpful comments. The *Fermi*-LAT Collaboration acknowledges generous ongoing support from a number of agencies and institutes that have supported both the development and the operation of the LAT as well as scientific

data analysis. These include the National Aeronautics and Space Administration and the Department of Energy in the United States, the Commissariat à l’Energie Atomique and the Centre National de la Recherche Scientifique / Institut National de Physique Nucléaire et de Physique des Particules in France, the Agenzia Spaziale Italiana and the Istituto Nazionale di Fisica Nucleare in Italy, the Ministry of Education, Culture, Sports, Science and Technology (MEXT), High Energy Accelerator Research Organization (KEK) and Japan Aerospace Exploration Agency (JAXA) in Japan, and the K. A. Wallenberg Foundation, the Swedish Research Council and the Swedish National Space Board in Sweden.

L. Costamante acknowledges partial support from the Grant “Cariplo/Regione Lombardia ID 2014-1980 / RST\_BANDO congiunto Fondazione Cariplo-Regione Lombardia - ERC”, for the project “Science and Technology at the frontiers of Gamma-Ray Astronomy with imaging atmospheric Cherenkov telescopes”.

We thank G. Ghisellini for useful discussions, in particular for pointing out the change in absorption shape due to the emission from a moving blob.

## REFERENCES

- Abdo A. A., et al., 2009, *ApJ*, **699**, 817  
 Abdo A. A., et al., 2010, *ApJ*, **721**, 1425  
 Abdo A. A., et al., 2011, *ApJ*, **733**, L26  
 Abolmasov P., Poutanen J., 2017, *MNRAS*, **464**, 152  
 Abramowski A., et al., 2013, *A&A*, **554**, A107  
 Acero F., et al., 2015, *ApJS*, **218**, 23  
 Acharya B. S., et al., 2013, *Astroparticle Physics*, **43**, 3  
 Ackermann M., et al., 2012a, *ApJS*, **203**, 4  
 Ackermann M., et al., 2012b, *Science*, **338**, 1190  
 Ackermann M., et al., 2015, *ApJ*, **810**, 14  
 Actis M., et al., 2011, *Experimental Astronomy*, **32**, 193  
 Aharonian F. A., 2004, Very high energy cosmic gamma radiation : a crucial window on the extreme Universe. World Scientific Publishing Co, doi:10.1142/4657  
 Aharonian F. A., Konopelko A. K., Völk H. J., Quintana H., 2001, *Astroparticle Physics*, **15**, 335  
 Aharonian F., et al., 2006, *Nature*, **440**, 1018  
 Aleksić J., et al., 2011, *ApJ*, **730**, L8  
 Aleksić J., et al., 2014, *A&A*, **569**, A46  
 Aleksić J., et al., 2016, *Astroparticle Physics*, **72**, 76  
 Atwood W. B., et al., 2009, *ApJ*, **697**, 1071  
 Bentz M. C., Peterson B. M., Pogge R. W., Vestergaard M., Onken C. A., 2006, *ApJ*, **644**, 133  
 Bentz M. C., et al., 2013, *ApJ*, **767**, 149  
 Bonnoli G., Ghisellini G., Foschini L., Tavecchio F., Ghirlanda G., 2011, *MNRAS*, **410**, 368  
 Böttcher M., Els P., 2016, *ApJ*, **821**, 102  
 Britto R. J., Bottacini E., Lott B., Razaque S., Buson S., 2016, *ApJ*, **830**, 162  
 Brown A. M., 2013, *MNRAS*, **431**, 824  
 Cao X., Jiang D. R., 1999, *MNRAS*, **307**, 802  
 Celotti A., Padovani P., Ghisellini G., 1997, *MNRAS*, **286**, 415  
 Chai B., Cao X., Gu M., 2012, *ApJ*, **759**, 114  
 Ciprini S., et al., 2007, in Ritz S., Michelson P., Meegan C. A., eds, American Institute of Physics Conference Series Vol. 921, The First GLAST Symposium, pp 546–547, doi:10.1063/1.2757444  
 Cleary K., Lawrence C. R., Marshall J. A., Hao L., Meier D., 2007, *ApJ*, **660**, 117  
 Costamante L., Tramacere A., Tosti G., Fermi LAT Collaboration 2010, in AAS/High Energy Astrophysics Division #11. p. 708  
 Damiani F., Maggio A., Micela G., Sciortino S., 1997, *ApJ*, **483**, 370  
 Domínguez A., et al., 2011, *MNRAS*, **410**, 2556  
 Donea A.-C., Protheroe R. J., 2003, *Astroparticle Physics*, **18**, 377

- Finke J. D., 2013, *ApJ*, **763**, 134
- Finke J. D., 2016, *ApJ*, **830**, 94
- Foschini L., Bonnoli G., Ghisellini G., Tagliaferri G., Tavecchio F., Stamerra A., 2013, *A&A*, **555**, A138
- Francis P. J., Hewett P. C., Foltz C. B., Chaffee F. H., Weymann R. J., Morris S. L., 1991, *ApJ*, **373**, 465
- Ghisellini G., Tavecchio F., 2008, *MNRAS*, **387**, 1669
- Ghisellini G., Tavecchio F., 2009, *MNRAS*, **397**, 985
- Ghisellini G., Tavecchio F., 2015, *MNRAS*, **448**, 1060
- Ghisellini G., Celotti A., Fossati G., Maraschi L., Comastri A., 1998, *MNRAS*, **301**, 451
- Ghisellini G., Tavecchio F., Foschini L., Ghirlanda G., Maraschi L., Celotti A., 2010, *MNRAS*, **402**, 497
- Ghisellini G., et al., 2011a, *MNRAS*, **411**, 901
- Ghisellini G., Tavecchio F., Foschini L., Ghirlanda G., 2011b, *MNRAS*, **414**, 2674
- Ghisellini G., Righi C., Costamante L., Tavecchio F., 2017, *MNRAS*, **469**, 255
- Helene O., 1984, *Nuclear Instruments and Methods in Physics Research A*, **228**, 120
- Holler M., et al., 2015, preprint, ([arXiv:1509.02902](https://arxiv.org/abs/1509.02902))
- Isler J. C., et al., 2013, *ApJ*, **779**, 100
- Isler J. C., et al., 2015, *ApJ*, **804**, 7
- Kaspi S., Brandt W. N., Maoz D., Netzer H., Schneider D. P., Shemmer O., 2007, *ApJ*, **659**, 997
- Khangulyan D. V., Barkov M. V., Bosch-Ramon V., Aharonian F. A., Dorodnitsyn A. V., 2013, *ApJ*, **774**, 113
- Lefa E., Kelner S. R., Aharonian F. A., 2012, *ApJ*, **753**, 176
- Lei M., Wang J., 2014, *PASJ*, **66**, 92
- León-Tavares J., et al., 2013, *ApJ*, **763**, L36
- Liu Y., Jiang D. R., Gu M. F., 2006, *ApJ*, **637**, 669
- Malmrose M. P., Marscher A. P., Jorstad S. G., Nikutta R., Elitzur M., 2011, *ApJ*, **732**, 116
- Marscher A. P., 2012, *International Journal of Modern Physics Conference Series*, **8**, 151
- Mattox J. R., et al., 1996, *ApJ*, **461**, 396
- Negrete C. A., Dultzin D., Marziani P., Sulentic J. W., 2013, *ApJ*, **771**, 31
- Nenkova M., Sirocky M. M., Ivezić Ž., Elitzur M., 2008, *ApJ*, **685**, 147
- Pacciani L., Tavecchio F., Donnarumma I., Stamerra A., Carrasco L., Recillas E., Porras A., Uemura M., 2014, *ApJ*, **790**, 45
- Peterson B. M., 2006, in Alloin D., ed., *Lecture Notes in Physics*, Berlin Springer Verlag Vol. 693, *Physics of Active Galactic Nuclei at all Scales*. p. 77, doi:10.1007/3-540-34621-X\_3
- Pian E., et al., 2006, *A&A*, **449**, L21
- Poutanen J., Stern B., 2010, *ApJ*, **717**, L118
- Protheroe R. J., Biermann P. L., 1997, *Astroparticle Physics*, **6**, 293
- Pushkarev A. B., Kovalev Y. Y., 2012, *A&A*, **544**, A34
- Romoli C., Taylor A. M., Aharonian F., 2017, *Astroparticle Physics*, **88**, 38
- Saito S., Stawarz Ł., Tanaka Y. T., Takahashi T., Madejski G., D'Ammando F., 2013, *ApJ*, **766**, L11
- Sbarrato T., Ghisellini G., Maraschi L., Colpi M., 2012, *MNRAS*, **421**, 1764
- Sbarrato T., Padovani P., Ghisellini G., 2014, *MNRAS*, **445**, 81
- Shaw M. S., et al., 2012, *ApJ*, **748**, 49
- Sikora M., Begelman M. C., Rees M. J., 1994, *ApJ*, **421**, 153
- Sikora M., Moderski R., Madejski G. M., 2008, *ApJ*, **675**, 71
- Sikora M., Stawarz Ł., Moderski R., Nalewajko K., Madejski G. M., 2009, *ApJ*, **704**, 38
- Stern B. E., Poutanen J., 2014, *ApJ*, **794**, 8
- Tavani M., Vittorini V., Cavaliere A., 2015, *ApJ*, **814**, 51
- Tavecchio F., Ghisellini G., 2008, *MNRAS*, **386**, 945
- Tavecchio F., Ghisellini G., 2012, preprint, ([arXiv:1209.2291](https://arxiv.org/abs/1209.2291))
- Tavecchio F., Becerra-Gonzalez J., Ghisellini G., Stamerra A., Bonnoli G., Foschini L., Maraschi L., 2011, *A&A*, **534**, A86
- Tavecchio F., Pacciani L., Donnarumma I., Stamerra A., Isler J., MacPherson E., Urry C. M., 2013, *MNRAS*, **435**, L24
- Torrealba J., Chavushyan V., Cruz-González I., Arshakian T. G., Bertone E., Rosa-González D., 2012, *Rev. Mex. Astron. Astrofis.*, **48**, 9
- Urry C. M., Padovani P., 1995, *PASP*, **107**, 803
- Vercellone S., et al., 2009, *ApJ*, **690**, 1018
- Vittorini V., Tavani M., Cavaliere A., Striani E., Vercellone S., 2014, *ApJ*, **793**, 98
- Xiong D. R., Zhang X., 2014, *MNRAS*, **441**, 3375

This paper has been typeset from a  $\text{\TeX}/\text{\LaTeX}$  file prepared by the author.

## APPENDIX A: ADDITIONAL TABLES AND FIGURES

Here we provide the complete version of Table A1 and Figures A1, A2 and A3. They are available to download as supplementary material on the electronic version of the journal.

**Table A1.** Spectral parameters of the fits of the gamma-ray SED data in Table 2. Col. [1]: object name. Col. [2]: redshift. Col. [3]: integral flux over the 0.2–10 GeV band, in  $\text{cm}^{-2} \text{s}^{-1}$ , from the logparabolic full-band model. Col. [4], [5], [6]: photon index, curvature and  $\chi_r^2$  of the best-fit model below 13 GeV rest-frame (Unabsorbed band). Col. [7], [8], [9]: photon index, curvature and  $\chi_r^2$  of the log-parabolic fit with BLR absorption (logptau), over the full LAT band and with all parameters free. Col. [10], [11]:  $\chi_r^2$  of the following fits over the full band: pure log-parabola with no BLR absorption (logp), power-law with high-energy cutoff with  $\beta_c = 1/3$  (exp03).

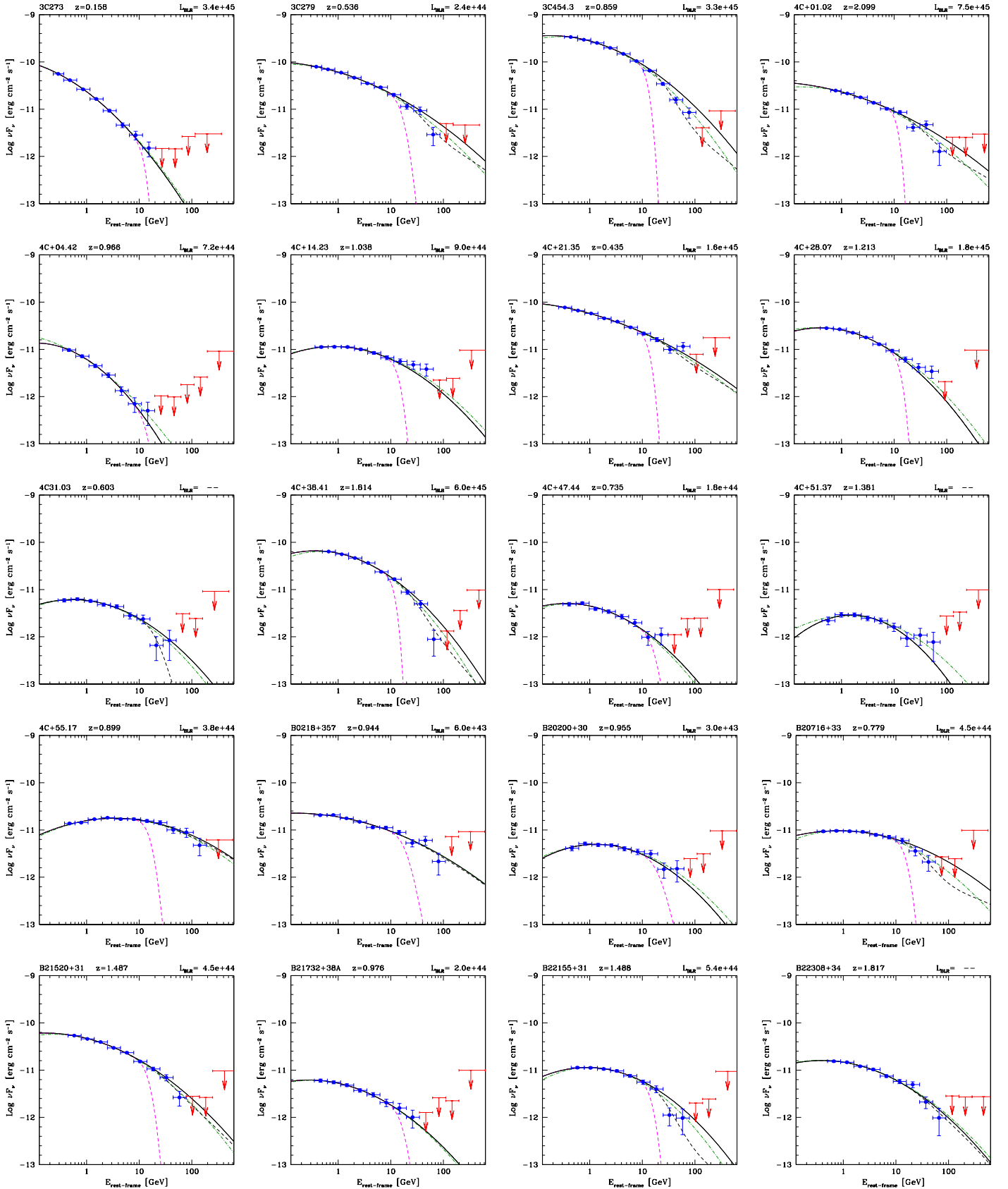
Name [1]	$z$ [2]	Flux 0.2-10 GeV [3]	GammaU [4]	betaU [5]	$\chi_r^2/\text{d.o.f.}$ [6]	GammaF [7]	betaF [8]	$\chi_r^2(\text{logptau})/\text{d.o.f.}$ [9]	$\chi_r^2(\text{logp})/\text{d.o.f.}$ [10]	$\chi_r^2(\text{exp03})/\text{d.o.f.}$ [11]
3C 454.3	0.859	8.49e-07	2.41±0.01	0.20±0.02	2.00/3	2.41±0.01	0.20±0.01	1.73/7	8.40/8	0.84/8
4C +21.35	0.435	1.94e-07	2.34±0.01	0.09±0.02	1.22/4	2.34±0.01	0.09±0.02	1.47/7	1.45/8	1.20/8
PKS 1510-08	0.36	3.47e-07	2.44±0.01	0.16±0.01	0.55/4	2.44±0.01	0.16±0.02	1.90/8	1.40/9	3.18/9
B2 1520+31	1.487	1.33e-07	2.42±0.02	0.18±0.04	1.81/3	2.42±0.01	0.17±0.03	1.48/6	1.83/7	0.92/7
PKS 1502+106	1.839	1.22e-07	2.26±0.02	0.20±0.05	2.89/3	2.25±0.02	0.20±0.05	2.47/6	3.47/7	2.07/7
PKS 0454-234	1.003	1.36e-07	2.22±0.01	0.18±0.03	1.35/4	2.22±0.01	0.17±0.03	2.07/7	2.47/8	1.82/8
3C 279	0.536	2.01e-07	2.37±0.01	0.12±0.02	1.26/4	2.38±0.01	0.13±0.03	1.21/7	1.62/8	1.22/8
3C 273	0.158	1.19e-07	2.86±0.01	0.24±0.03	0.35/4	2.86±0.01	0.24±0.03	0.42/5	0.32/6	0.71/6
PKS 2326-502	0.518	1.33e-07	2.29±0.01	0.24±0.03	1.09/4	2.29±0.01	0.23±0.03	1.45/6	6.11/7	2.73/7
PKS B1424-418	1.552	2.28e-07	2.13±0.01	0.16±0.02	1.41/3	2.13±0.02	0.17±0.04	3.56/7	4.84/8	1.44/8
PKS 1830-211	2.507	1.63e-07	2.46±0.01	0.09±0.02	0.10/2	2.48±0.01	0.14±0.03	0.80/6	1.02/7	0.45/7
4C +55.17	0.899	4.57e-08	1.91±0.02	0.17±0.07	2.08/3	1.91±0.02	0.16±0.04	1.26/8	1.01/9	0.90/9
PKS 0727-11	1.589	9.91e-08	2.27±0.02	0.12±0.04	1.06/3	2.26±0.02	0.11±0.05	1.89/6	2.27/7	1.43/7
4C +28.07	1.213	7.39e-08	2.40±0.01	0.27±0.02	0.30/3	2.40±0.02	0.26±0.03	0.76/6	0.53/7	1.25/7
PKS 0402-362	1.417	5.97e-08	2.70±0.04	0.45±0.07	1.50/3	2.69±0.03	0.43±0.07	1.45/4	1.19/5	1.40/5
Ton 599	0.725	4.61e-08	2.26±0.03	0.21±0.07	2.29/4	2.26±0.03	0.19±0.07	1.86/7	1.50/8	1.86/8
PKS 1244-255	0.635	6.78e-08	2.30±0.01	0.27±0.03	0.48/4	2.29±0.01	0.26±0.03	0.45/6	0.42/7	0.49/7
4C +38.41	1.814	1.59e-07	2.48±0.02	0.27±0.04	1.82/3	2.47±0.02	0.27±0.04	1.47/6	2.41/7	1.21/7
PMN J2345-1555	0.621	6.98e-08	2.04±0.01	0.17±0.03	1.10/4	2.04±0.01	0.18±0.03	0.75/7	0.87/8	0.71/8
S4 0917+44	2.19	3.13e-08	2.29±0.02	0.17±0.05	0.31/2	2.31±0.03	0.22±0.06	0.84/5	0.85/6	0.59/6
PKS 2052-47	1.491	5.32e-08	2.48±0.01	0.32±0.02	0.10/3	2.48±0.02	0.32±0.05	1.38/6	0.96/7	1.69/7
PKS 1124-186	1.048	6.36e-08	2.18±0.01	0.14±0.02	0.15/3	2.18±0.01	0.14±0.03	0.69/7	0.55/8	0.63/8
PKS 2142-75	1.138	6.21e-08	2.43±0.01	0.16±0.02	0.08/3	2.43±0.01	0.14±0.02	0.15/5	0.92/6	0.42/6
B3 1343+451	2.534	6.42e-08	2.20±0.03	0.16±0.05	0.87/2	2.20±0.01	0.15±0.03	0.64/7	0.59/8	0.34/8
PKS 0805-07	1.837	4.8e-08	2.13±0.01	0.15±0.04	0.41/3	2.11±0.03	0.12±0.06	1.59/6	1.90/7	1.10/7
PKS 0244-470	1.385	3.39e-08	2.43±0.03	0.14±0.07	1.01/3	2.44±0.02	0.15±0.05	0.70/5	0.65/6	0.48/6
CTA 102	1.037	8.41e-08	2.41±0.03	0.29±0.06	1.64/3	2.42±0.02	0.31±0.04	1.31/6	1.03/7	1.39/7
4C +01.02	2.099	6.19e-08	2.40±0.02	0.11±0.04	0.61/3	2.42±0.03	0.14±0.07	1.46/6	1.28/7	1.30/7
4C +14.23	1.038	3.3e-08	2.18±0.01	0.23±0.02	0.07/3	2.17±0.02	0.19±0.05	0.72/6	0.66/7	0.64/7
PKS 0250-225	1.427	4.31e-08	2.35±0.03	0.18±0.06	0.90/3	2.35±0.02	0.19±0.04	0.59/6	0.49/7	0.60/7
B2 2308+34	1.817	4.08e-08	2.36±0.02	0.21±0.04	0.49/3	2.34±0.02	0.17±0.06	1.11/6	0.91/7	1.06/7
B2 0716+33	0.779	2.81e-08	2.10±0.01	0.15±0.02	0.11/3	2.10±0.01	0.15±0.02	0.20/6	0.46/7	0.18/7
MG1 J123931+0443	1.762	6.34e-08	2.35±0.01	0.17±0.02	0.17/3	2.35±0.01	0.16±0.03	1.16/6	2.06/7	1.45/7
PMN J1802-3940	1.319	3.75e-08	2.11±0.05	0.30±0.11	3.18/4	2.11±0.04	0.31±0.11	2.40/6	2.01/7	2.61/7
S4 1849+67	0.657	3.18e-08	2.25±0.01	0.20±0.01	0.05/4	2.24±0.01	0.20±0.01	0.45/6	0.21/7	0.31/7
PKS 2023-07	1.388	4.86e-08	2.36±0.02	0.38±0.03	0.42/4	2.36±0.02	0.38±0.05	1.29/6	1.05/7	1.87/7

Table A1 – continued

Name [1]	$z$ [2]	Flux 0.2-10 GeV [3]	GammaU [4]	betaU [5]	$\chi_r^2$ /d.o.f. [6]	GammaF [7]	betaF [8]	$\chi_r^2$ (logptau)/d.o.f. [9]	$\chi_r^2$ (logp)/d.o.f. [10]	$\chi_r^2$ (exp03)/d.o.f. [11]
PKS 1454-354	1.424	3.64e-08	2.26±0.04	0.23±0.10	2.15/3	2.26±0.03	0.22±0.07	1.56/6	1.25/7	1.50/7
B3 1708+433	1.027	2.51e-08	2.27±0.03	0.36±0.07	0.73/3	2.27±0.03	0.34±0.08	1.83/6	1.33/7	1.97/7
GB6 J0742+5444	0.72	2.12e-08	2.22±0.04	0.29±0.08	1.49/4	2.22±0.03	0.28±0.07	1.57/6	1.25/7	1.52/7
OX 169	0.213	5.27e-08	2.53±0.02	0.18±0.04	0.50/4	2.53±0.02	0.18±0.04	0.92/6	0.69/7	0.95/7
PKS 2227-08	1.56	4.91e-08	2.80±0.03	0.24±0.06	0.55/3	2.79±0.03	0.22±0.05	0.52/4	0.42/5	0.45/5
PKS 2255-282	0.926	3.63e-08	2.49±0.04	0.33±0.09	1.40/3	2.49±0.04	0.35±0.08	1.35/5	1.10/6	1.38/6
B2 2155+31	1.488	3.22e-08	2.24±0.01	0.26±0.03	0.17/3	2.23±0.02	0.25±0.05	1.31/6	1.12/7	1.10/7
PKS 1622-253	0.786	7.28e-08	2.42±0.02	0.16±0.04	0.41/3	2.41±0.01	0.15±0.03	0.64/6	0.45/7	0.45/7
PKS 0420-01	0.916	3.62e-08	2.29±0.05	0.23±0.12	2.54/3	2.29±0.04	0.22±0.08	1.61/6	1.27/7	1.63/7
OC 457	0.859	3.83e-08	2.26±0.01	0.17±0.03	0.31/3	2.25±0.01	0.15±0.03	0.23/6	0.30/7	0.22/7
PKS 2201+171	1.076	2.55e-08	2.25±0.03	0.41±0.07	0.62/3	2.24±0.05	0.39±0.11	2.32/6	1.12/7	1.82/7
OP 313	0.997	3.1e-08	2.26±0.01	0.0	0.19/4	2.29±0.02	0.06±0.05	0.81/7	0.72/8	0.67/8
TXS 0059+581	0.644	3.05e-08	2.14±0.06	0.37±0.12	4.18/5	2.14±0.06	0.37±0.14	3.67/6	3.07/7	4.30/7
S4 1030+61	1.401	2.52e-08	2.15±0.02	0.13±0.04	0.43/3	2.16±0.01	0.15±0.03	0.30/6	0.40/7	0.27/7
OG 050	1.254	4.43e-08	2.32±0.04	0.19±0.09	1.79/3	2.30±0.03	0.14±0.07	1.26/6	1.09/7	1.14/7
PKS 0440-00	0.844	3.72e-08	2.39±0.01	0.12±0.01	0.04/3	2.40±0.02	0.14±0.03	0.92/6	0.41/7	0.37/7
PKS 1329-049	2.15	4.94e-08	2.65±0.04	0.33±0.10	1.74/3	2.64±0.04	0.33±0.09	2.14/6	1.72/7	2.02/7
TXS 1700+685	0.301	2.62e-08	2.32±0.03	0.20±0.06	1.07/4	2.33±0.03	0.22±0.06	0.89/6	0.75/7	0.89/7
S4 1144+40	1.089	3.83e-08	2.39±0.01	0.19±0.02	0.23/4	2.38±0.02	0.18±0.04	0.95/7	0.56/8	0.97/8
B0218+357	0.944	5.7e-08	2.26±0.03	0.11±0.07	3.15/4	2.26±0.03	0.12±0.06	2.45/7	2.12/8	2.47/8
PKS 0215+015	1.715	1.87e-08	2.06±0.03	0.0	0.51/3	2.08±0.04	0.08±0.09	1.04/6	1.39/7	1.04/7
PKS 0336-01	0.85	3.4e-08	2.41±0.04	0.22±0.09	1.28/3	2.40±0.03	0.20±0.06	1.36/6	0.90/7	1.06/7
4C 31.03	0.603	1.74e-08	2.24±0.02	0.25±0.05	0.42/4	2.24±0.03	0.27±0.08	1.91/6	1.15/7	1.34/7
OM 484	0.334	1.41e-08	2.31±0.02	0.0	0.27/5	2.31±0.02	0.01±0.05	1.76/5	1.73/6	1.23/6
TXS 1920-211	0.874	1.57e-08	2.00±0.07	0.43±0.19	2.47/3	1.98±0.06	0.35±0.12	1.71/5	2.38/6	1.92/6
MG2 J101241+2439	1.805	1.55e-08	2.32±0.05	0.0	2.13/5	2.27±0.07	0.00±0.16	2.23/4	5.68/5	4.61/5
S5 1044+71	1.15	5.09e-08	2.30±0.01	0.18±0.03	0.38/3	2.29±0.01	0.16±0.02	1.10/6	1.47/7	0.69/7
PMN J0850-1213	0.566	1.54e-08	2.14±0.05	0.33±0.11	1.39/4	2.14±0.05	0.31±0.10	1.27/6	0.96/7	1.22/7
PKS 0601-70	2.409	2.94e-08	2.66±0.12	0.34±0.22	2.66/2	2.66±0.10	0.33±0.20	3.05/5	1.32/6	1.50/6
B3 0650+453	0.933	1.52e-08	2.32±0.05	0.26±0.12	1.01/3	2.28±0.05	0.17±0.11	1.32/6	0.95/7	1.09/7
PKS 2320-035	1.393	3.82e-08	2.47±0.04	0.0	1.66/4	2.48±0.04	0.00±0.08	1.52/5	3.96/6	3.21/6
PKS 0736+01	0.18941	3.53e-08	2.54±0.03	0.24±0.08	1.05/4	2.54±0.03	0.25±0.07	1.57/6	1.29/7	1.59/7
PKS 1954-388	0.63	2.64e-08	2.37±0.03	0.18±0.07	1.04/4	2.37±0.03	0.17±0.06	0.81/5	1.65/6	0.89/6
TXS 1206+549	1.345	1.36e-08	2.48±0.06	0.0	1.67/4	2.51±0.06	0.12±0.13	1.32/4	1.63/5	1.40/5
B2 0200+30	0.955	1.4e-08	2.09±0.03	0.28±0.07	0.34/3	2.08±0.03	0.25±0.07	0.46/6	0.38/7	0.53/7
PKS 1730-13	0.902	4.39e-08	2.27±0.01	0.17±0.03	0.12/3	2.27±0.01	0.16±0.02	0.14/6	0.35/7	0.12/7
TXS 0106+612	0.783	2.85e-08	2.62±0.07	0.49±0.15	1.45/3	2.62±0.07	0.49±0.15	1.89/4	0.89/5	0.91/5
PKS 0528+134	2.07	2.51e-08	2.59±0.08	0.57±0.19	1.75/3	2.59±0.09	0.57±0.21	1.93/3	1.94/4	1.55/4
PKS 0446+11	2.153	2.7e-08	2.58±0.05	0.33±0.10	0.46/2	2.57±0.03	0.33±0.08	0.38/5	0.28/6	0.44/6
B2 1732+38A	0.976	1.57e-08	2.37±0.01	0.22±0.03	0.09/3	2.36±0.01	0.20±0.03	0.31/5	0.15/6	0.13/6
PKS 0130-17	1.02	1.54e-08	2.55±0.04	0.29±0.10	0.59/3	2.55±0.06	0.29±0.14	1.72/5	0.94/6	1.08/6
MRC 1659-621	1.75	1.84e-08	2.31±0.05	0.16±0.13	1.11/3	2.31±0.06	0.15±0.16	2.36/4	1.61/5	1.32/5
S5 0836+71	2.218	2.59e-08	3.12±0.09	0.56±0.15	1.15/2	3.12±0.09	0.56±0.14	2.40/4	1.84/5	2.34/5
PKS 0906+01	1.024	2.65e-08	2.48±0.04	0.24±0.10	1.06/3	2.47±0.04	0.23±0.08	0.71/5	0.57/6	0.73/6

Table A1 – continued

Name [1]	$z$ [2]	Flux 0.2-10 GeV [3]	GammaU [4]	betaU [5]	$\chi_r^2$ /d.o.f. [6]	GammaF [7]	betaF [8]	$\chi_r^2(\log\tau)$ /d.o.f. [9]	$\chi_r^2(\log p)$ /d.o.f. [10]	$\chi_r^2(\exp 03)$ /d.o.f. [11]
PKS 2123-463	1.67	1.37e-08	2.45±0.06	0.0	1.16/4	2.48±0.09	0.11±0.19	2.12/4	1.13/5	1.11/5
MG2 J071354+1934	0.54	1.75e-08	2.38±0.05	0.27±0.12	1.44/4	2.38±0.06	0.28±0.13	1.57/4	1.75/5	1.51/5
PMN J1344-1723	2.49	1.5e-08	2.08±0.03	0.0	0.20/2	2.21±0.08	0.11±0.23	2.49/6	2.10/7	2.08/7
TXS 0529+483	1.162	1.81e-08	2.30±0.05	0.30±0.13	1.22/3	2.30±0.05	0.29±0.11	1.31/5	1.08/6	1.35/6
PKS 1551+130	1.308	1.72e-08	2.43±0.06	0.0	2.38/5	2.43±0.08	0.10±0.18	2.19/5	1.82/6	1.81/6
S3 0458-02	2.291	2.95e-08	2.36±0.03	0.26±0.06	0.29/2	2.35±0.02	0.24±0.06	0.49/5	0.41/6	0.51/6
PKS B1908-201	1.119	3.07e-08	2.32±0.03	0.27±0.07	0.54/3	2.33±0.02	0.28±0.05	0.36/5	0.31/6	0.33/6
MG2 J201534+3710	0.859	8.76e-08	2.46±0.02	0.24±0.05	0.41/3	2.46±0.02	0.22±0.04	0.43/6	0.30/7	0.55/7
CTS 0490	0.36	1.16e-08	2.13±0.04	0.53±0.08	0.59/4	2.13±0.04	0.53±0.09	0.59/4	0.50/5	0.57/5
PKS 0451-28	2.564	1.84e-08	2.70±0.13	0.30±0.25	2.45/2	2.72±0.09	0.33±0.19	1.67/3	2.88/4	1.86/4
4C +47.44	0.735	1.35e-08	2.36±0.04	0.26±0.08	0.74/4	2.36±0.04	0.26±0.10	1.07/5	0.78/6	0.70/6
PKS 0235-618	0.465	1.03e-08	2.32±0.06	0.0	1.72/5	2.33±0.07	0.16±0.17	1.79/4	1.43/5	1.54/5
4C +04.42	0.966	2.02e-08	2.93±0.03	0.37±0.06	0.16/3	2.93±0.05	0.37±0.10	1.81/4	1.26/5	1.42/5
PKS 0454-46	0.858	1.46e-08	2.60±0.07	0.16±0.14	1.03/3	2.60±0.06	0.15±0.13	1.52/5	0.96/6	1.00/6
S4 1726+45	0.717	1.48e-08	2.51±0.04	0.33±0.10	0.79/4	2.50±0.05	0.32±0.11	0.94/4	0.72/5	0.86/5
PKS 0142-278	1.148	1.18e-08	2.72±0.11	0.45±0.23	1.96/3	2.72±0.12	0.45±0.25	2.94/4	2.15/5	2.21/5
PKS 2144+092	1.113	2.18e-08	2.56±0.05	0.32±0.12	1.03/3	2.56±0.05	0.32±0.12	1.92/4	0.75/5	0.86/5
S4 1851+48	1.25	9.28e-09	2.07±0.06	0.39±0.14	1.32/4	2.06±0.08	0.36±0.18	2.04/5	1.38/6	1.73/6
PKS 1118-05	1.297	1.59e-08	2.37±0.08	0.29±0.19	2.21/3	2.36±0.06	0.26±0.15	1.73/4	1.37/5	1.52/5
4C +51.37	1.381	7.93e-09	2.15±0.04	0.41±0.09	0.29/3	2.15±0.05	0.40±0.12	1.73/6	1.32/7	1.59/7
PKS 0208-512	1.003	3.45e-08	2.35±0.05	0.18±0.12	3.29/3	2.34±0.04	0.16±0.08	2.60/4	2.83/5	2.08/5
TXS 0322+222	2.066	1.84e-08	2.71±0.06	0.0	1.22/4	2.70±0.09	0.01±0.19	2.02/2	2.12/3	1.95/3
PKS B1127-145	1.184	9.13e-09	2.70±0.06	0.19±0.13	0.34/3	2.70±0.06	0.19±0.14	0.36/3	0.45/4	0.48/4
CRATES J0303-6211	1.348	5.18e-09	2.22±0.08	0.0	0.86/4	2.25±0.10	0.22±0.25	0.89/3	0.69/4	0.75/4
PMN J1617-5848	1.422	1.01e-08	2.46±0.13	0.0	1.82/4	2.46±0.17	0.00±0.44	2.45/3	1.83/4	1.83/4
CRATES J1613+3412	1.397	6.97e-09	2.43±0.07	0.40±0.17	0.89/4	2.43±0.11	0.40±0.28	1.99/4	1.86/5	2.09/5



**Figure A1.** Average *Fermi*-LAT spectra (SED) plotted in the source rest frame energy, listed in alphabetical order. Upper limits are at the  $2\sigma$  level (see text). Solid lines show the fit of the spectrum with parameters determined below 13 GeV. Dashed lines show the spectrum with BLR absorption fitted to the data, using the solid-line spectrum as intrinsic model. When  $L_{\text{BLR}}$  is available, the magenta dashed line shows the expected absorbed spectrum if the emitting region is located at  $R_{\text{diss}} = R_{\text{BLR}}/2$ . Dot-dashed (green) lines show the fit of a pure log-parabolic model to the whole spectrum.

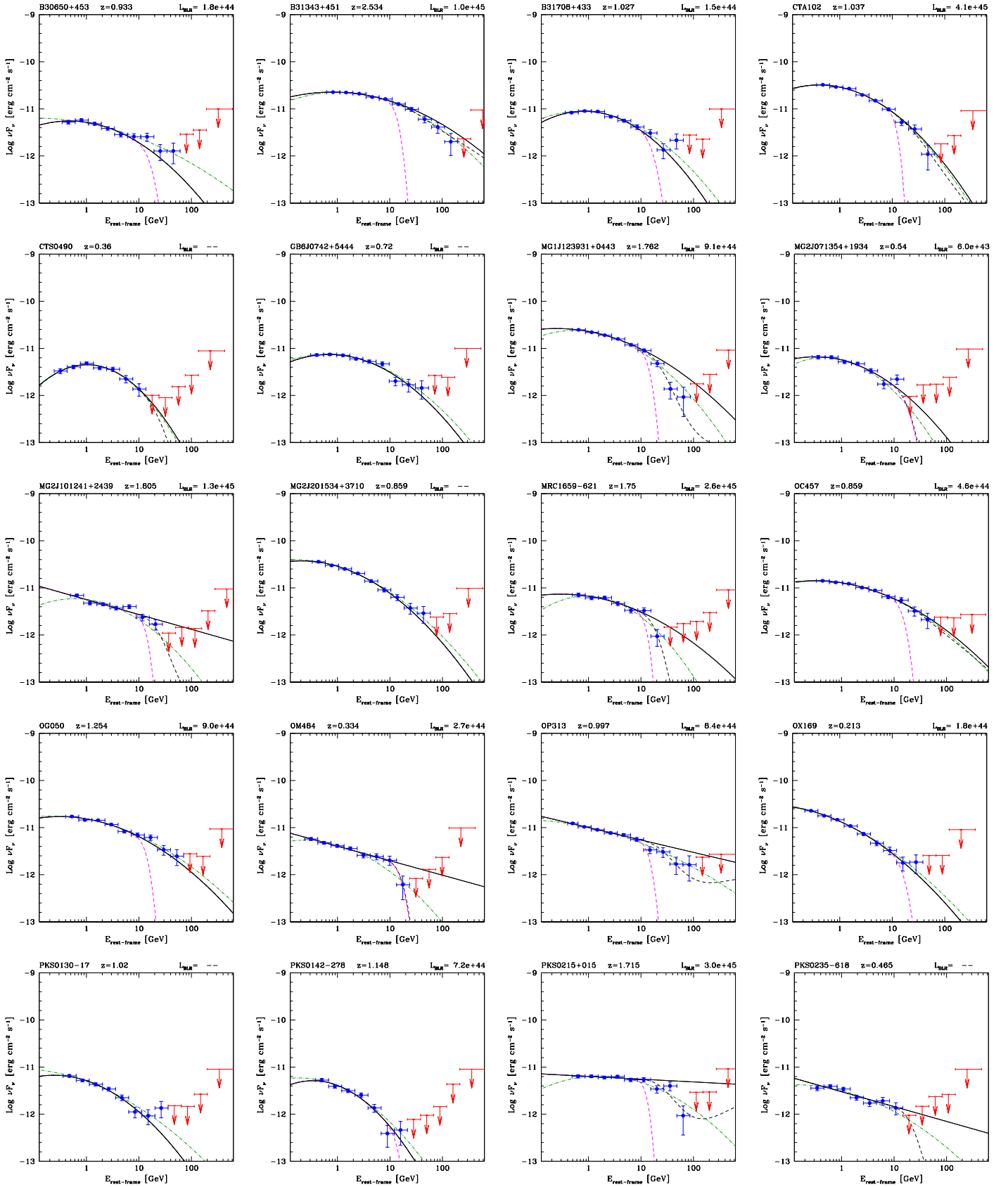


Figure A1 – continued

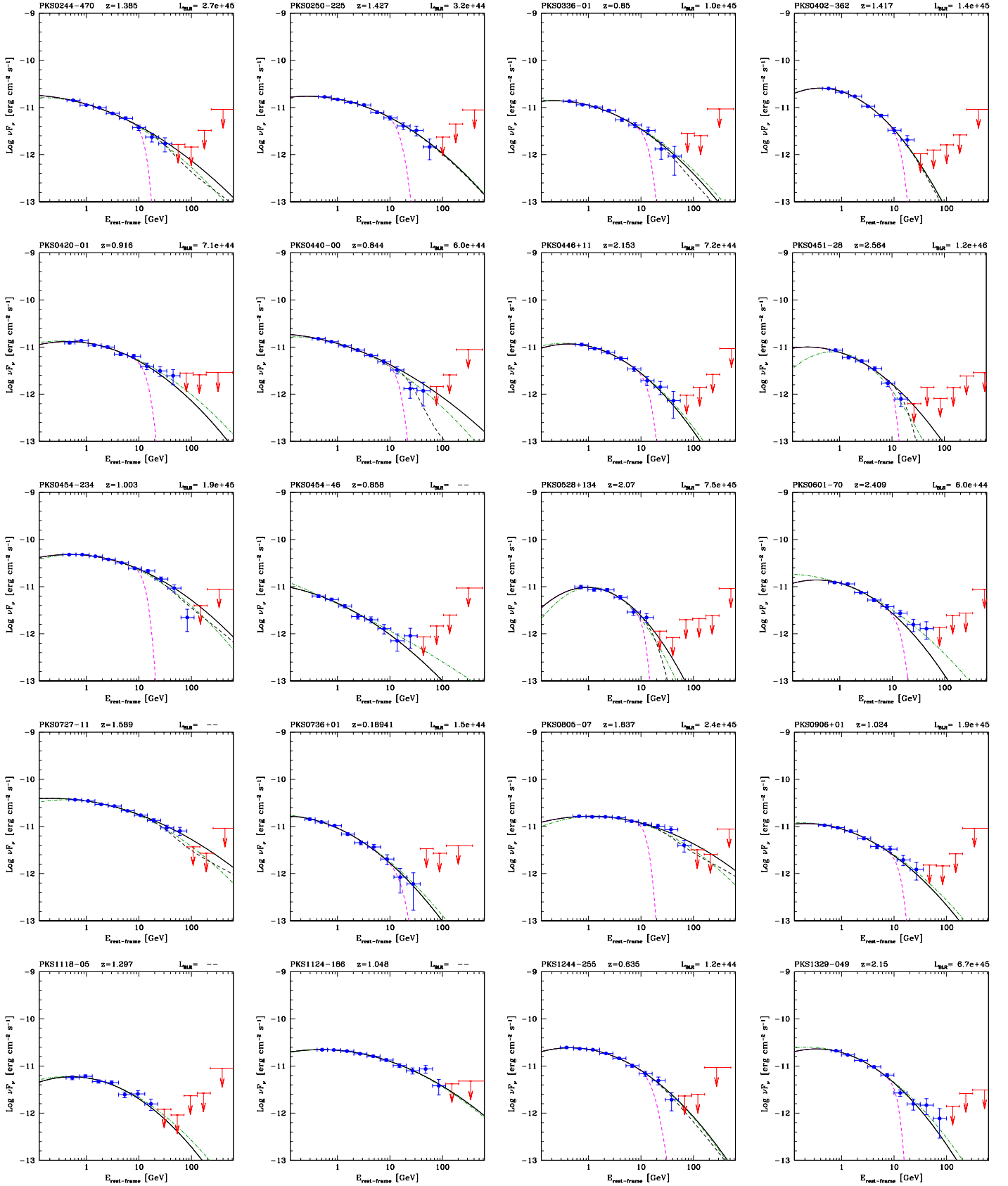


Figure A1 – continued

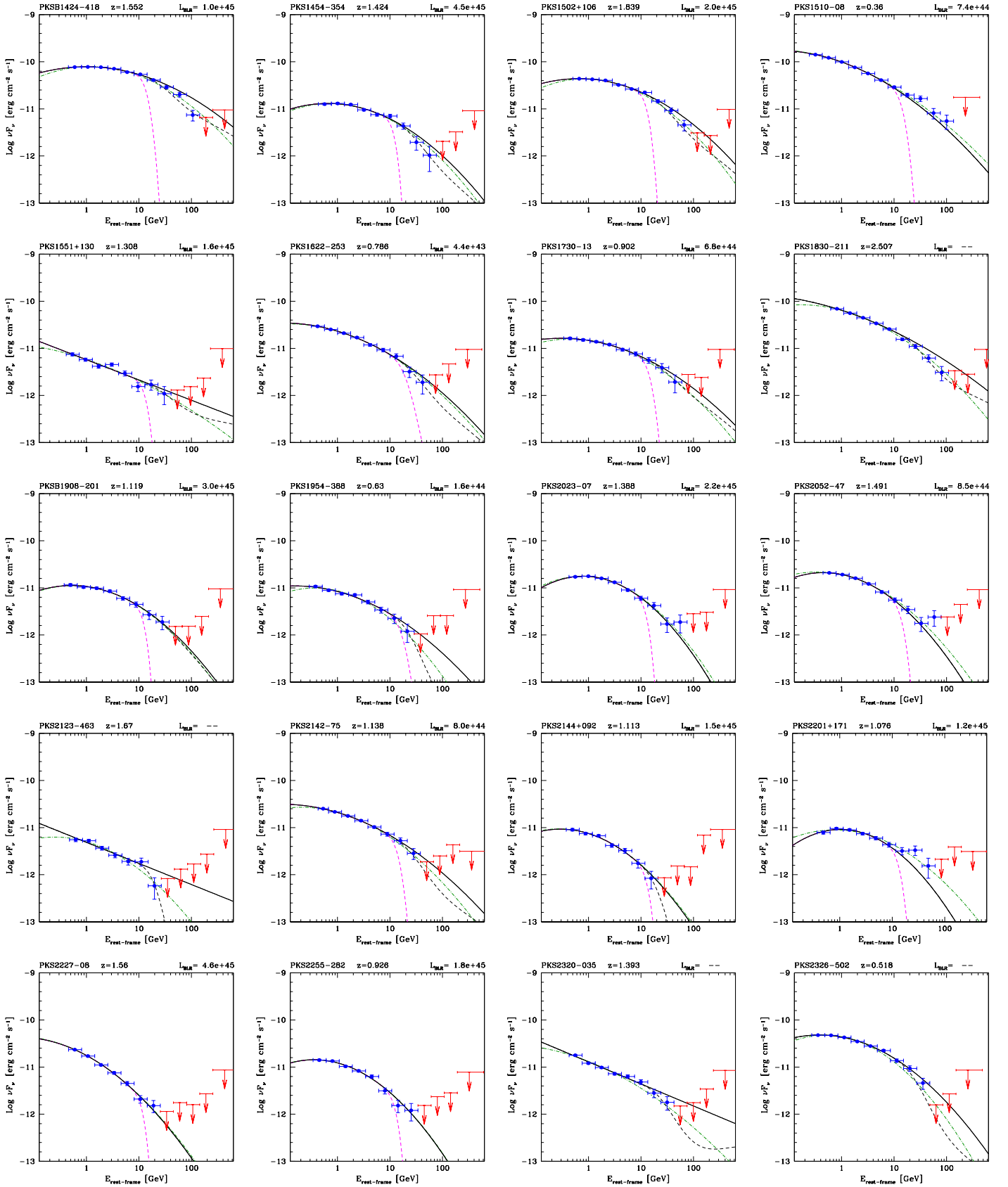


Figure A1 – continued

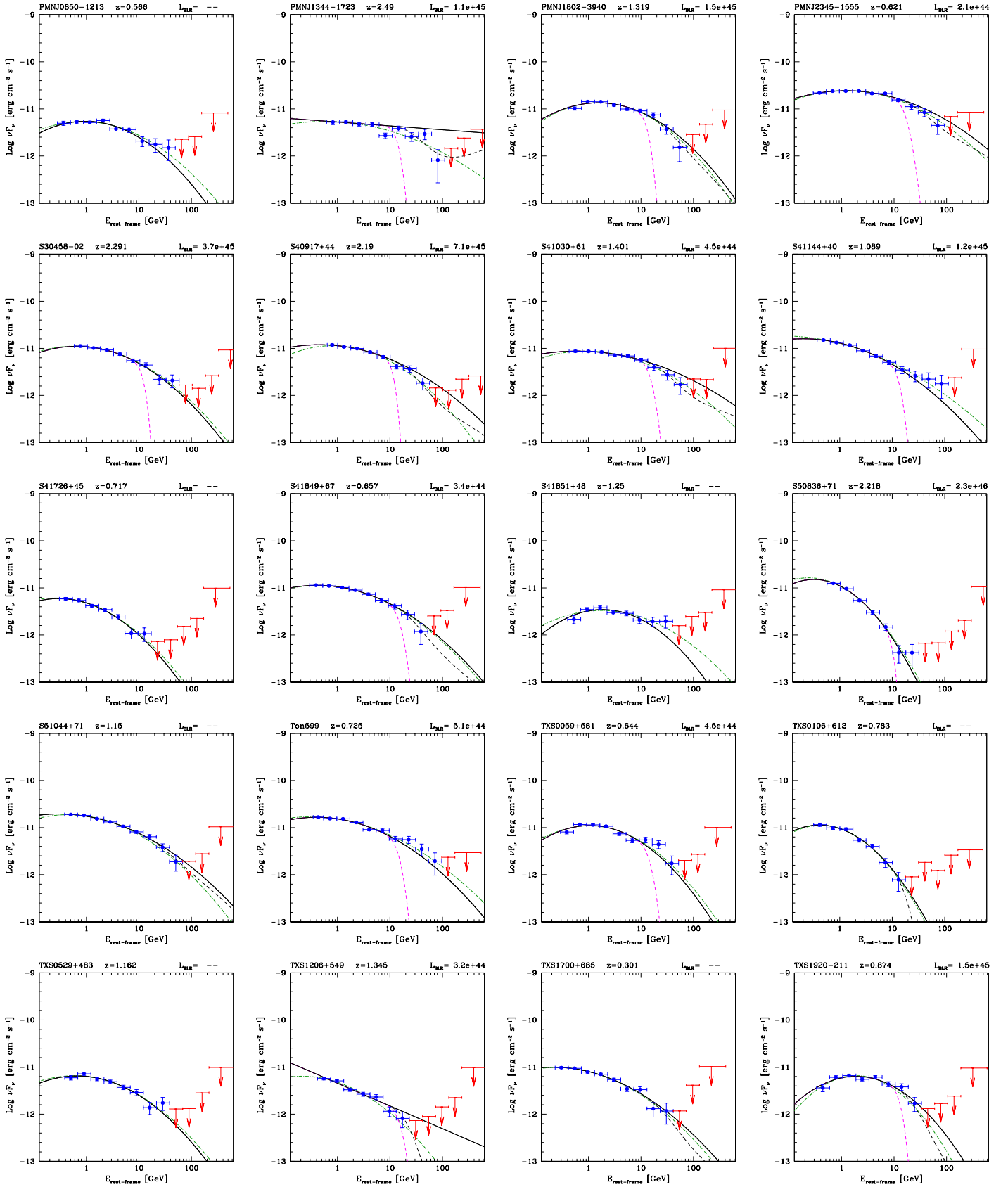
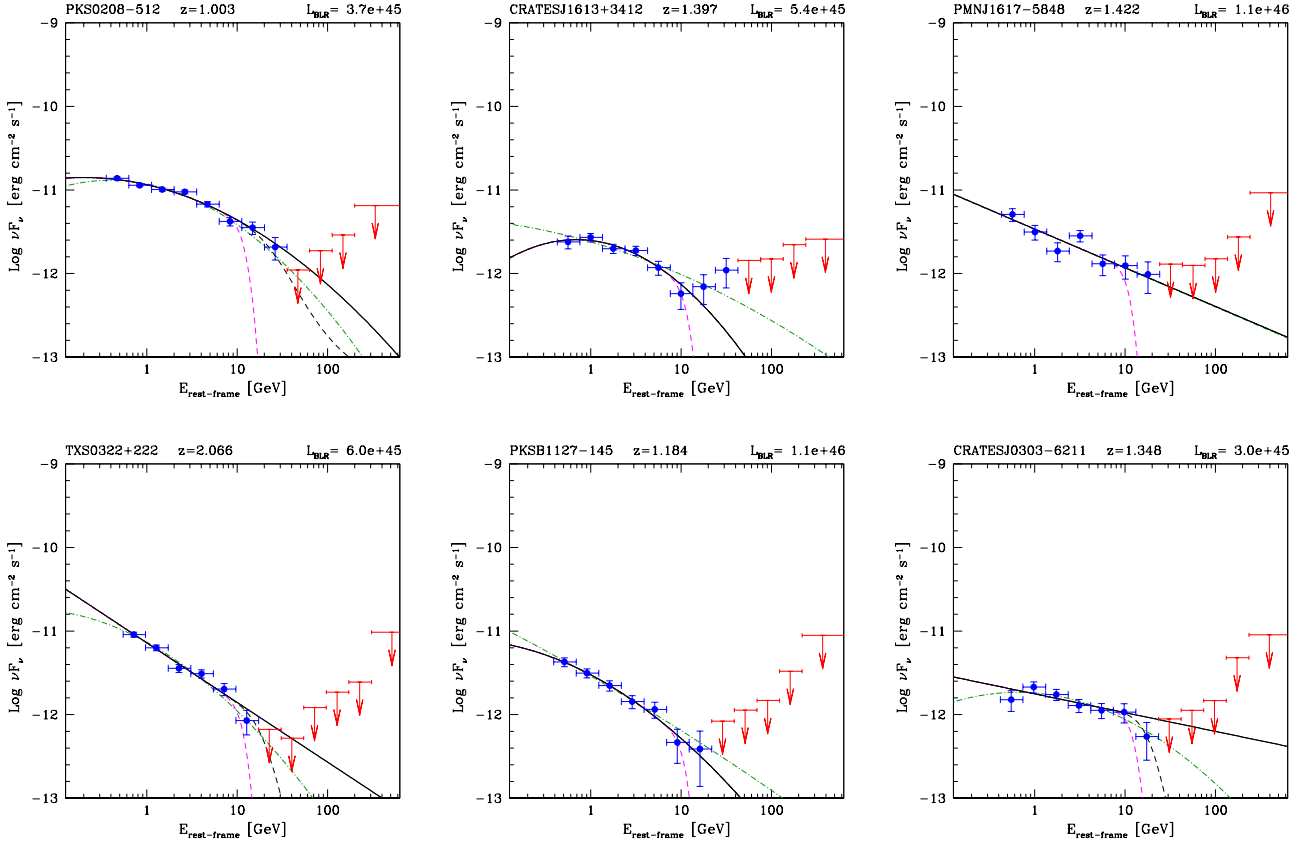
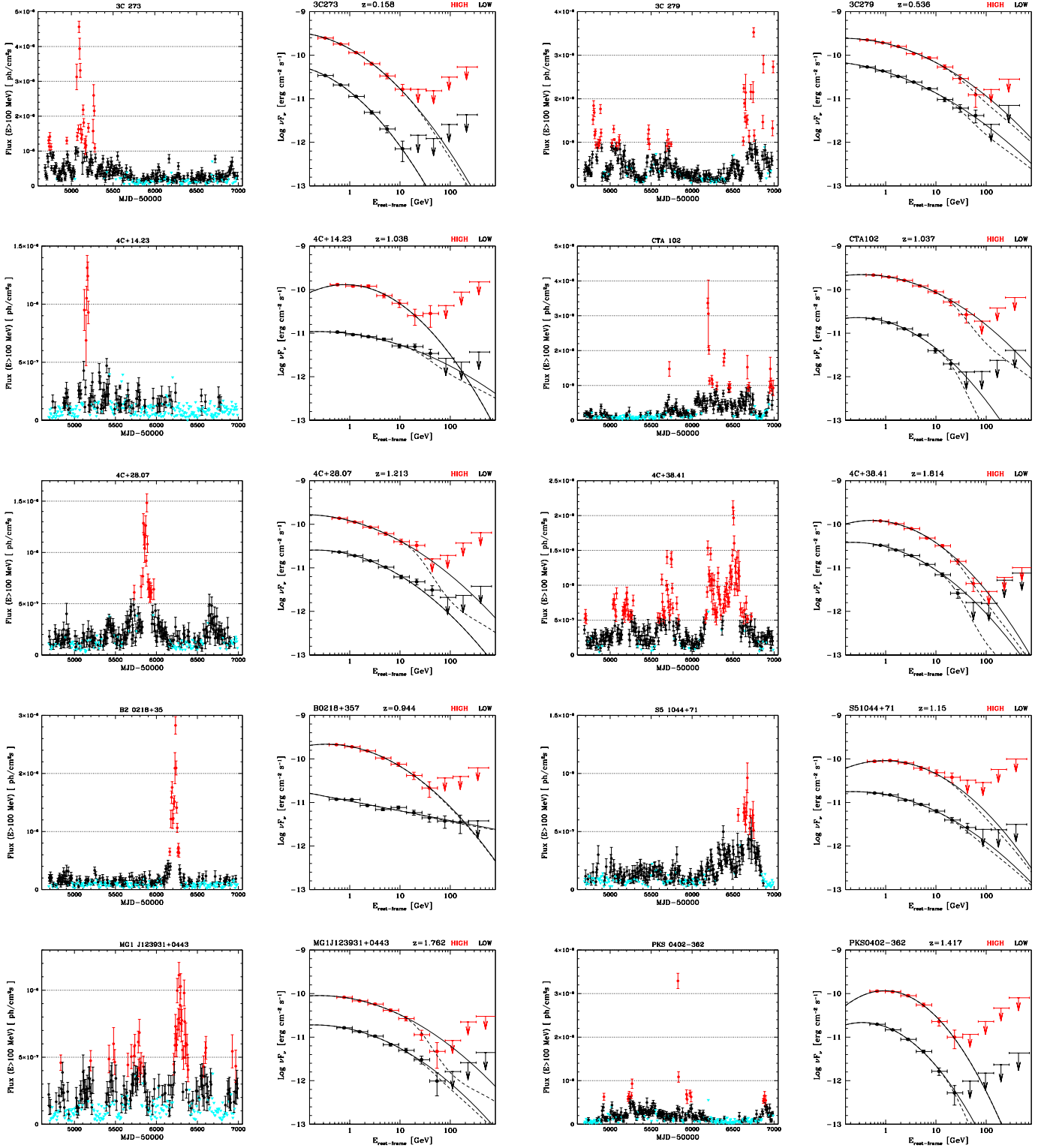


Figure A1 – continued



**Figure A2.** Spectra of the additional FSRQ with large BLR. Upper row: data are constraining, showing a lower BLR absorption than expected. Lower row: data are not conclusive.



**Figure A3.** Lightcurves and gamma-ray SEDs of the FSRQ which have been divided in an average High (red) and Low-state (black) spectra. Lightcurves: time binning is 7-day bins. High-state bins are marked in red, Low-state bins in black or cyan. Cyan triangles correspond to upper limits, for the bins when the source is not detected in the 7-days timespan. Spectra: full lines show the intrinsic spectrum with parameters determined below 13 GeV, dashed lines show the result of BLR absorption applied to the intrinsic spectrum and fitted to the data, with free optical depth.

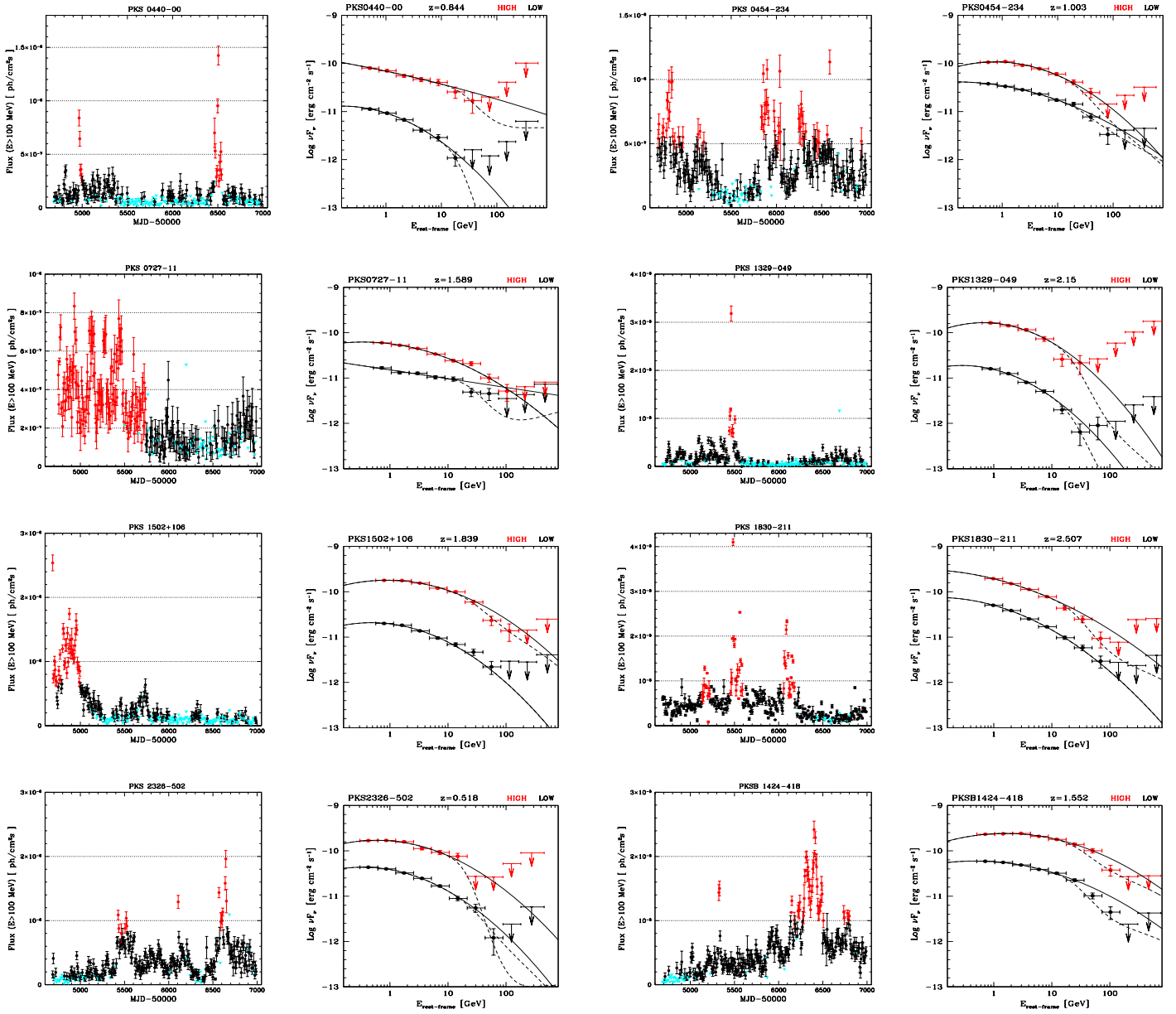


Figure A3 – continued